

# Optimization of active drag reduction for a slanted Ahmed body in a high-dimensional parameter space

**Yiqing Li<sup>1,2</sup>, Wenshi Cui<sup>1,2</sup>, Qing Jia<sup>1,2</sup>, Qiliang Li<sup>1,2</sup>, Zhigang Yang<sup>1,2,3</sup> and Bernd R. Noack<sup>4,5†</sup>**

<sup>1</sup> Shanghai Automotive Wind Tunnel Center, Tongji University, 4800 CaoAn Road, Jiading District, Shanghai 201804

<sup>2</sup> Shanghai Key Lab of Vehicle Aerodynamics and Vehicle Thermal Management Systems, Shanghai 201804, China

<sup>3</sup> Beijing Aeronautical Science & Technology Research Institute, Beijing, 102211, China

<sup>4</sup> LIMSI, CNRS, Université Paris-Saclay, Bât 507, rue du Belvédère, Campus Universitaire, F-91403 Orsay, France

<sup>5</sup>Hermann-Föttinger-Institut, Technische Universität Berlin, Müller-Breslau-Straße 8, D-10623 Berlin, Germany

(Received ?; revised ?; accepted ?. - To be entered by editorial office)

We numerically optimize drag of the 35° slanted Ahmed body with active flow control using Reynolds-Averaged Navier-Stokes simulations (RANS). The Reynolds number is  $Re_H = 1.9 \times 10^5$  based on the height of the Ahmed body. The wake is controlled with seven local jet slot actuators at all trailing edges. Symmetric operation corresponds to five independent actuator groups at top, middle, bottom, top sides and bottom sides. Each slot actuator produces a uniform jet with the velocity and angle as free parameters. The drag is reduced by 17% optimizing all 10 actuation parameters as free input. The optimal actuation emulates boat tailing by inward-directed blowing with velocities which are comparable to the oncoming velocity. The results are well aligned with an experimental drag reduction of a square Ahmed body by boat tailing with using Coanda actuation (Barros *et al.* 2016). A key enabler for the optimization task is an algorithm which alternates between downhill simplex iteration for the exploitation of the best discovered local minima and Latin hypercube sampling for the exploration of possibly better minima. The combined algorithm is shown to be more efficient than the purely explorative and exploitative components. The optimization iteration is analyzed as control landscape with a proximity map. This map gives a two-dimensional impression of the drag topology in the 10-dimensional parameter space. We expect that the combination of RANS simulations, the proposed optimization algorithm and the control landscape analysis may guide many future active flow control plants.

## 1. Introduction

In this study, we focus on active drag reduction behind a generic car model using Reynolds-averaged Navier-Stokes (RANS) simulations. Aerodynamic drag is a major contribution of traffic-related costs, from airborne to ground and marine traffic. A small drag reduction would have a dramatic economic effect considering that transportation accounts for approximately 20% of global energy consumption, Gad-el Hak (2006); Kim (2011). While the drag of airplanes and ships is largely caused by skin-friction, the

† Email address for correspondence: zhigangyang@tongji.edu.cn, bernd.noack@limsi.fr

resistance of cars and trucks is mainly caused by pressure or bluff-body drag. (Hucho 2002) defines bodies with a pressure drag exceeding the skin-friction contribution as bluff and as streamlined otherwise.

The pressure drag of cars and trucks originates from the excess pressure at the front scaling with the dynamic pressure and a low-pressure region at the rear side of lower but negative magnitude. The reduction of the pressure contribution from the front side often requires significant changes of the aerodynamic design. Few active control solutions for the front drag reduction have been suggested Minelli *et al.* (2016). In contrast, the contribution at the rearward side can significantly be changed with passive or active means. Drag reductions of 10% to 20% are common, (Pfeiffer & King 2014) have even achieved 25% drag reduction with active blowing. For a car at a speed of 120km/h, this would reduce consumption by about 1.8 liter per 100 km. The economic impact of drag reduction is significant for trucking fleets with a profit margin of only 2-3%. Two thirds of the operating costs are from fuel consumption. Hence, a 5% reduction of fuel costs from aerodynamic drag corresponds to over 100% increase of the profit margin.

The car and truck design is largely determined by practical and aesthetic considerations. In this study, we focus on drag reduction by passive or active means at the rearward side. Intriguingly most drag reductions of bluff body fall in the categories of Kirchhoff solution and aerodynamic boat tailing. The first strategy may be idealized by the Kirchhoff solution, i.e. potential flow around the car with infinitely thin shear-layers from the rearward separation lines, separating the oncoming flow and a dead-water region. The low-pressure region due to curved shear-layers is replaced by an elongated, ideally infinitely long wake with small, ideally vanishing curvature of the shear-layer. This wake elongation is achieved by reducing entrainment through the shear-layer, e.g. by phasor-control control mitigating vortex shedding (Pastoor *et al.* 2008) or by energetization of the shear-layer with high-frequency elongation (Barros *et al.* 2016). Wake disrupters also decrease drag, yet by energetizing the shear layer (Park *et al.* 2006) or delaying separation (Aider *et al.* 2010). Arguably, the drag of the Kirchhoff solution can be considered as achievable limit with small actuation energy.

The second strategy targets drag reduction by aerodynamic boat tailing. Geropp (1995); Geropp & Odenthal (2000) have pioneered this approach by Coanda blowing. Here, the shear-layer originating at the bluff body is vectored inward and gives thus rise to a more streamlined wake shape. Barros *et al.* (2016) has achieved 20% drag reduction of a square-back Ahmed body with high-frequency Coanda blowing in a high-Reynolds-number experiment. A similar drag reduction was achieved with steady blowing but at higher  $C_\mu$  values.

This study focuses on drag reduction of the low-drag Ahmed body with rear slant angle of 35 degrees. This Ahmed body idealizes the shape of many cars. (Bideaux *et al.* 2011; Gilliéron & Kourta 2013) have achieved 20% drag reduction for this configuration in an experiment. High-frequency blowing was applied orthogonal to the upper corner of the slanted rear surface. Intriguingly, the maximum drag reduction was achieved in a narrow range of frequencies and actuation velocities and its effect rapidly deteriorated for slightly changed parameters. In addition, the actuation is neither Coanda blowing nor an ideal candidate for shear-layer energization.

The literature on active drag reduction of the Ahmed body indicates that small changes of actuation can significantly change its effectiveness. Actuators have been applied with beneficial effects at all rearward edges (Barros *et al.* 2016), thus further complicating the optimization task. A systematic optimization of the actuation at all edges, including amplitudes and angles of blowing, is beyond reach of current experiments. In this study, a systematic RANS optimization is performed in a rich parametric space comprising the

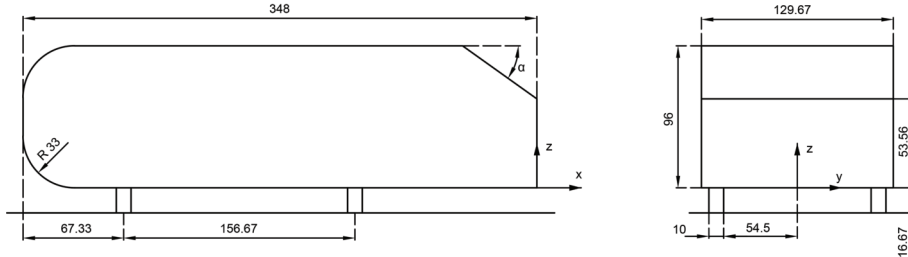


FIGURE 1. Dimensions of the investigated 1:3-scaled Ahmed body. *a*) Side view. *b*) Back view. The length unit is mm and the angle is specified in degrees.

angles and amplitudes of steady blowing of five actuator groups: one the top, middle and bottom edge and two symmetric actuators at the corners of the slanted and vertical surface. High-frequency forcing is not considered, as the RANS tends to be overly dissipative to the actuation response.

The choice of optimization algorithm is critical for an acceptable computational load. A simple gradient search, like the downhill simplex method, may provide a drag minimum in many dozens of simulations, but there is no guarantee for a global minimum. On the other hand, exploratory strategies, like Monte Carlo methods or Latin hypercube sampling, will eventually come close to the global minimum, but tend to be prohibitively expensive. In this study, we combine exploitation and exploration in a single novel explorative gradient search strategy.

The goal of the current study is a simulation-based optimization of actuation for the low-drag Ahmed body. The manuscript is organized as follows. § 2 describes the configuration and RANS simulation. The employed optimization algorithms are introduced in § 3. § 4, 5, and 6 describe the optimization for the one-, five- and ten-dimensional actuation space, respectively. The first one-dimensional space contains the streamwise velocity of the top jet actuator. The five-dimensional space comprises the streamwise velocities of the 5 symmetric actuators. And the ten-dimensional space includes in addition to these velocities also the orientation angle. Our results are summarized in § 7.

## 2. Configuration and RANS simulation

Starting point of the computational fluid dynamics plant is an experimental study of a low-drag  $35^\circ$  Ahmed body (Li *et al.* 2018). The investigated Ahmed body configuration (§ 2.1) has the same physical dimensions. The effect of actuation is assessed with a Reynolds-Averaged Navier-Stokes (RANS) simulation (§ 2.2). The companion experiment is briefly recapitulated in § 2.3.

### 2.1. Configuration

Point of departure is an experimentally investigated 1:3-scaled Ahmed body characterized by slanted edge angle of  $\alpha = 35^\circ$  with length  $L$ , width  $W$  and height  $H$  of 348mm, 130mm and 96mm, respectively. The front edges are rounded with a radius of  $0.344H$ . The model is placed on four cylindrical supports with a diameter equal to 10 mm and the ground clearance is  $0.177H$ . The origin of the Cartesian coordinate system  $(x, y, z)$ , is located in the symmetry plane on the lower edge of the model's vertical base (see figure 1). Here,  $x$ ,  $y$  and  $z$  denote the streamwise, spanwise and wall-normal coordinate, respectively. The velocity components in the  $x$ ,  $y$  and  $z$  directions are denoted by  $u$ ,  $v$  and  $w$ , respectively. The free-stream velocity is chosen to be  $U_\infty = 30$  m/s.

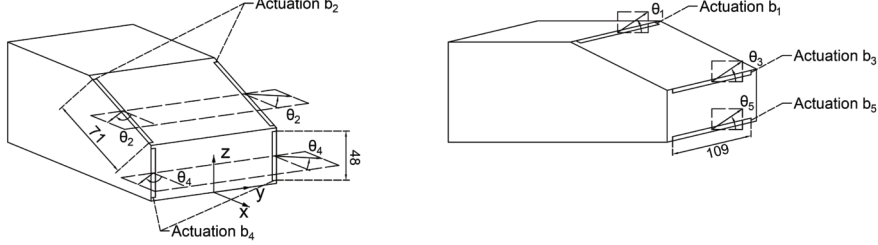


FIGURE 2. Deployment and blowing direction of actuators on the rear window and the vertical base. The angles  $\theta_1, \theta_2, \theta_3, \theta_4$  and  $\theta_5$  are all defined to be positive when pointing outward or upward.

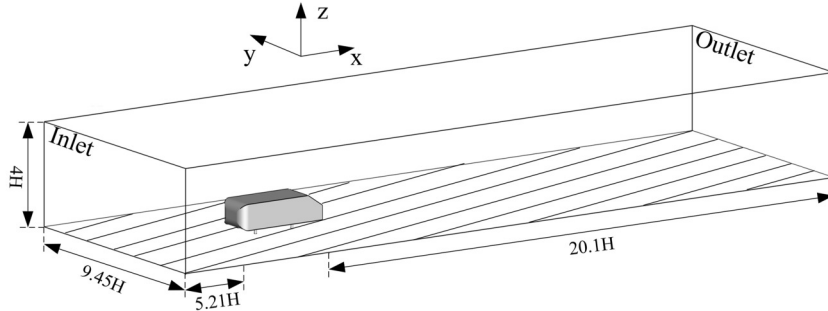


FIGURE 3. Computational domain of the RANS simulation.

Five groups of steadily blowing slot actuators (figure 2) are deployed on all edges of the rear window and the vertical base. All slot widths are 2 mm. The horizontal actuators at the top, middle and bottom side have lengths of 109 mm. The upper and lower sidewise actuators on the upper and vertical rear window have a length of 71 mm and 48 mm, respectively. The actuation velocities  $U_1, \dots, U_5$  are independent parameters.  $U_1$  refers to the upper edge of the rear window,  $U_3$  to the middle edge and  $U_5$  to the lower edge of the vertical base.  $U_2$  and  $U_4$  correspond to the velocities at the right and left sides of the upper and lower window, respectively.

Following the experiment by Zhang *et al.* (2018), all blowing angles can be varied as indicated in figure 2. This study aims at minimizing drag as represented by the drag coefficient,  $J = c_D$ , by varying the actuation control parameters. The actuation velocity amplitudes  $U_i, i = 1, \dots, 5$  are capped by twice of the single optimum value as discussed in § 4. The actuation angles  $\theta_i, i = 1, \dots, 5$  are fixed to  $0^\circ$ , i.e. streamwise direction, in a 5-dimensional optimization. The actuation angles are later added into the input parameters in 10-dimensional optimization, with variable angles  $\theta_1 \in [-35^\circ, 90^\circ]$ ,  $\theta_2, \theta_3, \theta_4, \theta_5 \in [-90^\circ, 90^\circ]$ .

## 2.2. Reynolds-Average Navier-Stokes (RANS) simulations

A numerical wind tunnel (figure 3) is constructed using the commercial grid generation software Ansys ICEM CFD. The rectangular computational domain is bounded by  $X_1 \leq x \leq X_2$ ,  $0 \leq z \leq H_T$ ,  $|y| \leq W_T/2$ . Here,  $X_1 = -5.21 H$ ,  $X_2 = 20.17 H$ ,  $H_T = 4H$ , and  $W_T = 9.45H$ . A coarse, medium and fine mesh using unstructured hexahedral computational grid are employed in order to evaluate the performance of RANS method for

Mesh grid points	2.5M	5M	10M
Drag Coefficient	0.294	0.313	0.318

TABLE 1. Drag coefficient based on different mesh resolutions.

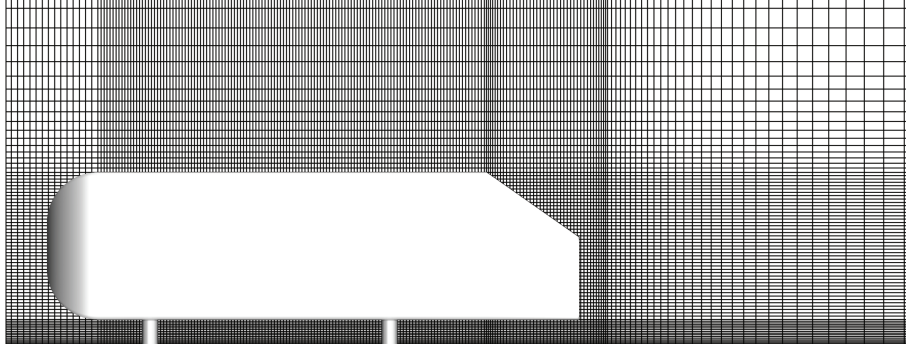


FIGURE 4. Side view of the computational grid used for RANS.

the current problem with different mesh resolutions. The statistics in Table 1 show that using a finer mesh can be expected to have negligible improvement on the accuracy of the drag coefficient. Hence, the more economical medium mesh 4 is used. This mesh consists of 5 million elements and features dimensionless wall values  $\Delta x^+ = 20$ ,  $\Delta y^+ = 3$ ,  $\Delta z^+ = 30$ . In addition to resolving the boundary layer, the shear layers and the near-wake region, the mesh near the actuation slots is also refined.

Reynolds-Averaged Navier-Stokes (RANS) simulations using the realizable  $k - \epsilon$  model with the constant parameters

$$\begin{aligned} \sigma_k &= 1.0, \sigma_\epsilon = 1.2, C_2 = 1.9 \\ C_1 &= \max \left( 0.43, \frac{\eta}{\eta + 5} \right) \\ \eta &= \left( 2 \sum_{i,j=1}^3 E_{ij} E_{ji} \right)^{1/2} \frac{k}{\epsilon} \\ E_{ij} &= \frac{1}{2} \left( \frac{\partial u_i}{\partial x_j} + \frac{\partial u_j}{\partial x_i} \right) \end{aligned}$$

$\sigma_k = 1.0$ ,  $\sigma_\epsilon = 1.2$ ,  $C_2 = 1.9$  are performed employing the commercial flow solver Ansys Fluent. The spatial discretization is based on a second-order upwind scheme in the form of SIMPLE scheme based on a pressure-velocity coupling method. RANS simulation have been frequently and successfully been used to assess actuation effects from steady blowing (Ben-Hamou *et al.* 2007; Dejoan *et al.* 2005; Muralidharan *et al.* 2013; Viken *et al.* 2003). We deem RANS simulations to provide reasonable qualitative and approximately quantitative indications for actuator optimization and plan an experimental validation in the future. Partially Averaged Navier-Stokes (PANS) simulations (Han *et al.* 2013) and Large Eddy Simulation (LES) (Krajinović 2009; Brunn & Nitsche 2006) are trusted higher-fidelity simulations for drag reduction with active flow control but are computationally orders of magnitudes more demanding.

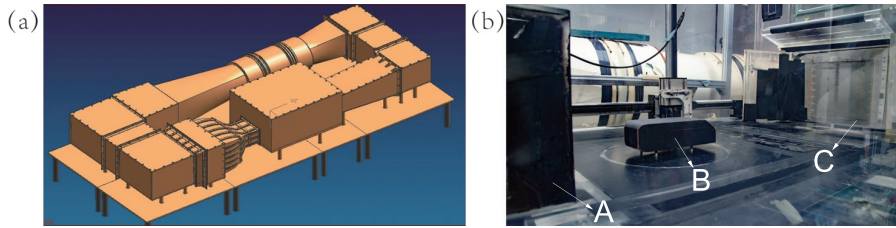


FIGURE 5. Experimental setup with the Ahmed body in the model wind tunnel (a). Photo (b) shows the open test section with the Ahmed body (B) linked to a six component balance. A is the wind-tunnel jet; C is its collector.

### 2.3. Companion experiment

The experiment was implemented in a scaled wind-tunnel with 3 : 4 open jet in the Shanghai Automotive Wind Tunnel Center (SAWTC) with an geometric blockage of approximately 10% (see figure 5). The Ahmed body was placed at the corresponding position in the wind tunnel as figure 3. The force measurement system consists of an external six-component balance, a balance platform, an Ahmed body model support system, a signal amplifier, a data collecting system and a data processing system. At an incoming velocity of 30 m/s, the drag coefficient obtained from the drag measurement is 0.3299 which is 5% larger than the RANS result. This difference may be attributed to the blockage effect, boundary-layer differences or RANS modeling inaccuracy. Details are provided by (Li *et al.* 2018).

The wake of the low-drag 35° slanted Ahmed body is numerically and experimentally found to be statistically symmetric without forcing and under symmetric forcing. This observations is consistent with other control studies of this slanted version (Krentel *et al.* 2012; Kourta & Leclerc 2013) and different from the observed bi-modal dynamics of the square back Ahmed body at high ground clearance (Grandemange *et al.* 2013; Östh *et al.* 2014; Barros *et al.* 2017; Evstafyeva *et al.* 2017).

## 3. Optimization algorithms

In this section, the employed optimization algorithms for the actuation parameters are described. Let  $J(\mathbf{b})$  be the cost function—here the drag coefficient—depending on  $N$  actuation parameters  $\mathbf{b} = (b_1, \dots, b_N)$  in the domain  $\Omega$ ,

$$\mathbf{b} = (b_1, \dots, b_N) \in \Omega \subset \mathcal{R}^N.$$

The optimization goal is to find the global minimum of  $J$  in  $\Omega$ ,

$$\mathbf{b}^* = \arg \min_{\mathbf{b} \in \Omega} J(\mathbf{b}). \quad (3.1)$$

Starting point is the downhill simplex algorithm (see, e.g. Press *et al.* 2007) as robust representative for gradient search (§ 3.1). This algorithm exploits gradient information from neighboring points to descent to a local minimum. In contrast, Latin hypercube sampling (LHS) (see, again Press *et al.* 2007) optimally explores the whole domain  $\Omega$  independently of the cost values, i.e. ignores any gradient information. Evidently, LHS has the larger chance of getting close to the global minimum while the simplex algorithm is more efficient descending down a minimum, potentially a suboptimal one. We exploit the advantages of the simplex method in exploiting a local minimum and the LHS in exploring the global one in a new *explorative gradient search algorithm* explained in § 3.3.

All algorithms are illustrated for a two-dimensional analytic cost function

$$J(b_1, b_2) = 1 - 0.5e^{-4(b_1-0.5)^2-4(b_2-0.5)^2} - e^{-4(b_1-1.5)^2-4(b_2-1.5)^2} \quad (3.2)$$

with the argument in square domain  $\Omega := \{(b_1, b_2) : 0 \leq b_1, b_2 \leq 2\}$ . The cost  $J$  has two minima, a local one  $J \approx 0.5$  near  $(0.5, 0.5)$  and a global one  $J \approx 0$  near  $(1.5, 1.5)$ .

§ 3.4 discusses the choice of the initial condition and a quantization of actuation for reducing the computational load of RANS computations.

### 3.1. Downhill simplex search

The downhill simplex method by Nelder & Mead (1965) is a very simple, robust and widely used gradient search algorithm. This method does not require any gradient information and is well suited for expensive function evaluations, like the considered RANS simulation for the drag coefficients, and for experimental optimizations with inevitable noise. A price is a slow convergence for the minimization of smooth functions as compared to algorithms which can exploit gradient and curvature information.

We briefly outline the employed downhill simplex algorithm, as there are many variants. First,  $N+1$  vertices  $\mathbf{b}_m$ ,  $m = 1, \dots, N+1$  in  $\Omega$  are initialized as detailed in the respective sections. Commonly,  $\mathbf{b}_1$  is placed somewhere in the middle of the domain and the other vertices explore steps in all directions,  $\mathbf{b}_m = \mathbf{b}_1 + h\mathbf{e}_{m-1}$ ,  $m = 2, \dots, N+1$ . Here,  $\mathbf{e}_i = (\delta_{i1}, \dots, \delta_{iN})$  is a unit vector in  $i$ -th direction and  $h$  is a step size which is small compared to the domain. Evidently, all vertices must remain in the domain  $\mathbf{b}_m \in \Omega$ .

The goal of the simplex transformation iteration is to replace the worst argument  $\mathbf{b}_h$  of the considered simplex by a new better one  $\mathbf{b}_{N+2}$ . This is archived in following steps:

**1) Ordering:** Without loss of generality, we assume that the vertices are sorted in terms of the cost values  $J_m = J(\mathbf{b}_m)$ :  $J_1 \leq J_2 \leq \dots \leq J_{N+1}$ .

**2) Centroid:** In the second step, the centroid of the best side opposite to the worst vertex  $\mathbf{b}_{N+1}$  is computed:

$$\mathbf{c} = \frac{1}{N} \sum_{m=1}^N \mathbf{b}_m.$$

**3) Reflection:** Reflect the worst simplex  $\mathbf{b}_{N+1}$  at the best side,

$$\mathbf{b}_r = \mathbf{c} + (\mathbf{c} - \mathbf{b}_{N+1})$$

and compute the new cost  $J_r = J(\mathbf{b}_r)$ . Take  $\mathbf{b}_r$  as new vertex, if  $J_1 \leq J_r \leq J_N$ .  $\mathbf{b}_m$ ,  $m = 1 \dots, N$  and  $\mathbf{b}_r$  define the new simplex for the next iteration. Renumber the indices to the  $1 \dots N+1$  range. Now, the cost is better than the second worst value  $J_N$ , but not as good as the best one  $J_1$ . Start a new iteration with step 1.

**4) Expansion:** If  $J_r < J_1$ , expand in this direction further by a factor 2,

$$\mathbf{b}_e = \mathbf{c} + 2(\mathbf{b}_{N+1} - \mathbf{c}).$$

Take the best vertex of  $\mathbf{b}_r$  and  $\mathbf{b}_e$  as  $\mathbf{b}_{N+1}$  replacement and start a new iteration.

**5) Single contraction:** At this stage,  $J_r \geq J_N$ . Contract the worst vertex half-way towards centroid,

$$\mathbf{b}_c = \mathbf{c} + (1/2)(\mathbf{c} - \mathbf{b}_{N+1}).$$

Take  $\mathbf{b}_c$  as new vertex ( $\mathbf{b}_{N+1}$  replacement), if it is better than the worst one, i.e.  $J_c \leq J_{N+1}$ . In this case, start the next iteration.

**6) Shrink / multiple contraction:** At this stage, none of the above operations was successful. Shrink the whole simplex by a factor 1/2 towards the best vertex, i.e. replace

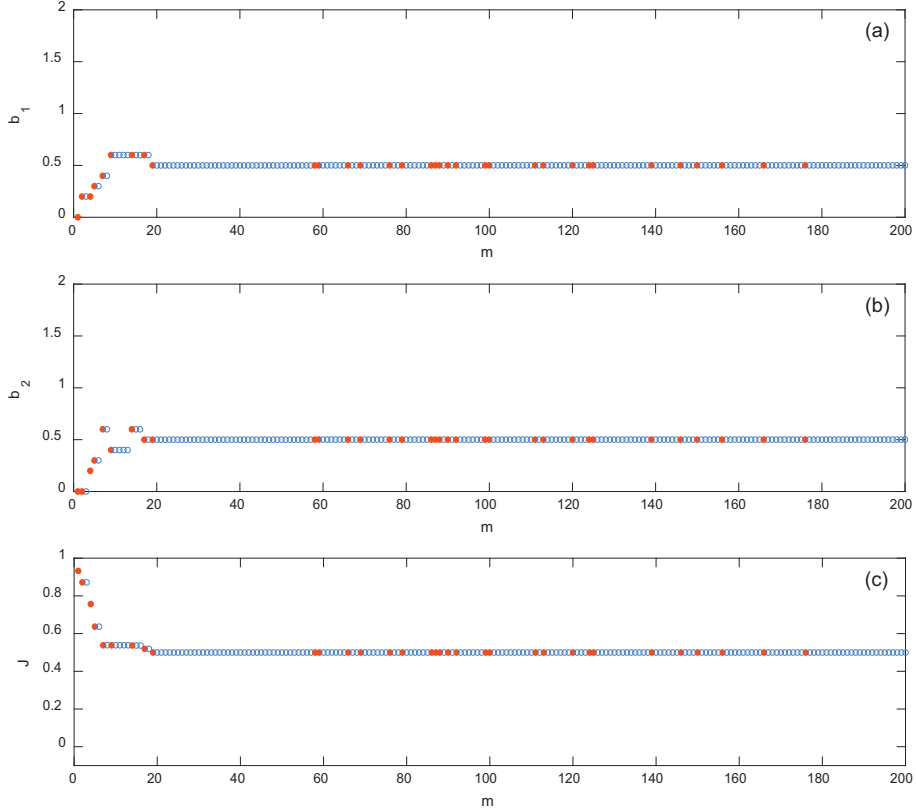


FIGURE 6. Downhill simplex algorithm applied to the test function (3.2). The figure shows the iteration of (a)  $b_1$ , (b)  $b_2$  and (c) the associated cost  $J$ . A red circle marks a newly discovered minimum, while blue circles indicate the best unchanged value of the simplex.  $m$  counts the evaluations of the cost function  $J$ .

all vertices by

$$\mathbf{b}_m \mapsto \mathbf{b}_1 + \frac{1}{2} (\mathbf{b}_m - \mathbf{b}_1), m = 2, \dots, N+1.$$

This shrunked simplex represents the one for the next iteration. It should be noted that this shrinking operation is the last resort as it is very expensive with  $N$  function evaluations. The rational behind this shrinking is that a smaller simplex may better follow local gradients.

Figure 6 illustrates the simplex algorithm for the analytical function (3.2) with the initial simplex  $\mathbf{b}_1 = (0, 0)$ ,  $\mathbf{b}_2 = (0, 0.2)$ ,  $\mathbf{b}_3 = (0.2, 0)$ . The simplex rapidly converges to a local minimum near  $(0.5, 0.5)$ . Figure 7 illustrates the evolution of the simplex in the parameter space.

### 3.2. Latin hypercube sampling

The downhill simplex method exploits neighbourhood information to slide down to a local minimum. Latin hypercube sampling (LHS) (McKay *et al.* 1979) aims to explore the parameter space irrespective of the cost values. We employ a space-filling variant which effectively covers the whole permissible domain of parameters. This explorative strategy ('maximin' criterion in Mathematica) minimizes the maximum minimal distance

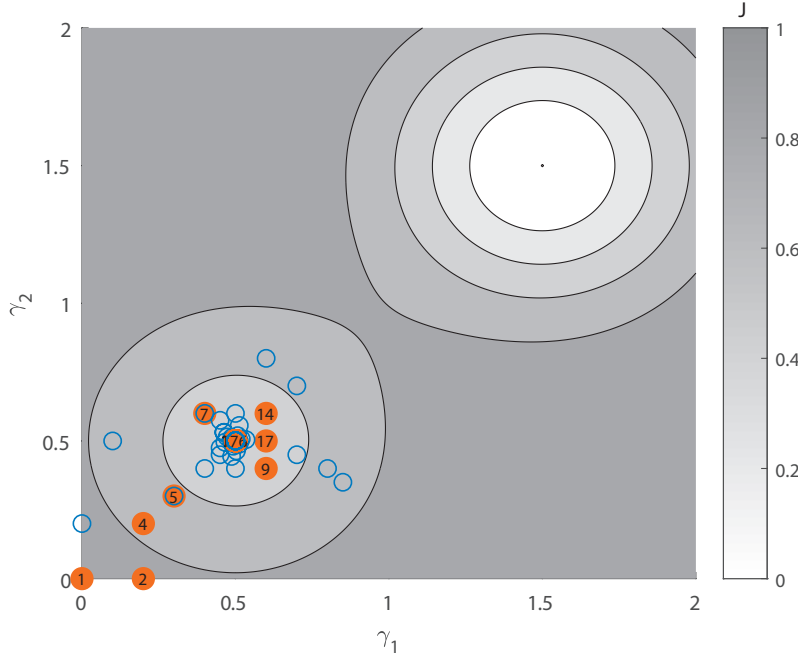


FIGURE 7. Same downhill simplex iteration as in figure 6, but displayed in the two-dimensional parameter space. Red solid circles mark new optima while blue open circles denote investigated suboptimal vertices. The numbers in the circles correspond to evaluation counter  $m$ .

between the points:

$$\{\mathbf{b}_m\}_{m=1}^M = \arg \max_{\mathbf{b}_m \in \Omega} \min_{\substack{i=1, \dots, M-1 \\ j=i+1, \dots, M}} \|\mathbf{b}_i - \mathbf{b}_j\|.$$

In other words, there is no other sampling of  $M$  parameters with a larger minimum distance.  $M$  can be any positive integral number.

For better comparison with the simplex algorithm, we employ an iterative variant. Note that once  $M$  sample points are created and they cannot be augmented anymore, for instance when learning of LHS was not satisfactory. We create a large number of LHS parameters  $\mathbf{b}_j^*$ ,  $j = 1, \dots, M^*$  for a dense coverage of the parameter space  $\Omega$  at the beginning, typically  $M^* = 10^6$ . As first sample  $\mathbf{b}_1$ , the center of the initial simplex is taken. The second parameter is taken from  $\mathbf{b}_j^*$ ,  $j = 1, \dots, M^*$  maximizing the distance to  $\mathbf{b}_1$ ,

$$\mathbf{b}_2 = \operatorname{argmax}_{\mathbf{b}_j^*, j=1, \dots, M^*} \|\mathbf{b}_j^* - \mathbf{b}_1\|.$$

The third parameter  $\mathbf{b}_3$  is taken from the same set so that the minimal distance to  $\mathbf{b}_1$  and  $\mathbf{b}_2$  is maximized and so on. This procedure allows to recursively refine sample points and to start with an initial set of parameters.

Figure 8 illustrates the LHS for the analytical test function. In contrast to the downhill simplex algorithm, LHS arrives near the global optimum at  $m = 15$ . From figure 9, the domain  $\Omega$  is nearly homogeneously covered with samples. The next significant improvement requires and much finer ‘resolution’ and orders of magnitudes more samples.

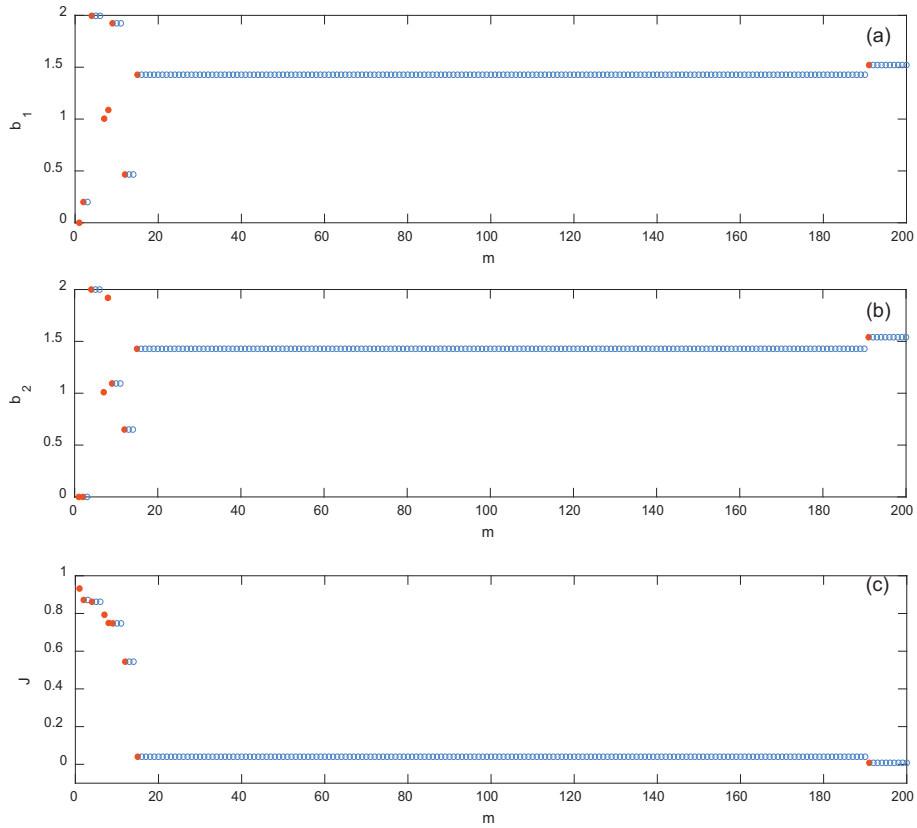


FIGURE 8. Same as figure 6, but for Latin Hypercube Sampling.

### 3.3. Explorative gradient search

In this section, we combine the advantages of the exploitative downhill simplex method and the explorative LHS in a single algorithm.

**Step 0—Initialize.** First,  $\mathbf{b}_m$ ,  $m = 1, \dots, M + 1$  are initialized for the downhill simplex algorithm.

**Step 1—LHS.** Compute the cost  $J$  of a new LHS parameter  $\mathbf{b}$ . As described above, we take a parameter from a precomputed list which is furthest away from all hitherto employed parameters.

**Step 2—Downhill Simplex.** Perform one simplex iteration (§3.1) with the best  $M + 1$  parameters discovered so far.

**Step 3—Loop.** Continue with Step 1 until a convergence criterion is met.

The algorithm is intuitively appealing. If the LHS discovers a parameter with a cost  $J$  in the top  $M + 1$  values, this parameter is included in the new simplex and corresponding iteration may slide down in another better minimum.

The explorative gradient search is applied to the test function starting with the same vertices  $\mathbf{b}_1$ ,  $\mathbf{b}_2$ ,  $\mathbf{b}_3$  as in § 3.1. Already in the first exploratory step, the algorithm quickly finds a more promising terrain near the global minimum (1.5, 1.5). The next iterations exploit this new minimum. From figure 7, the explorative steps are seen to cover the whole parameter space. As the global minimum has been found, the exploration slows down convergence. This is the inevitable price for avoiding the descend into the suboptimal local minimum and not using any knowledge about the terrain.

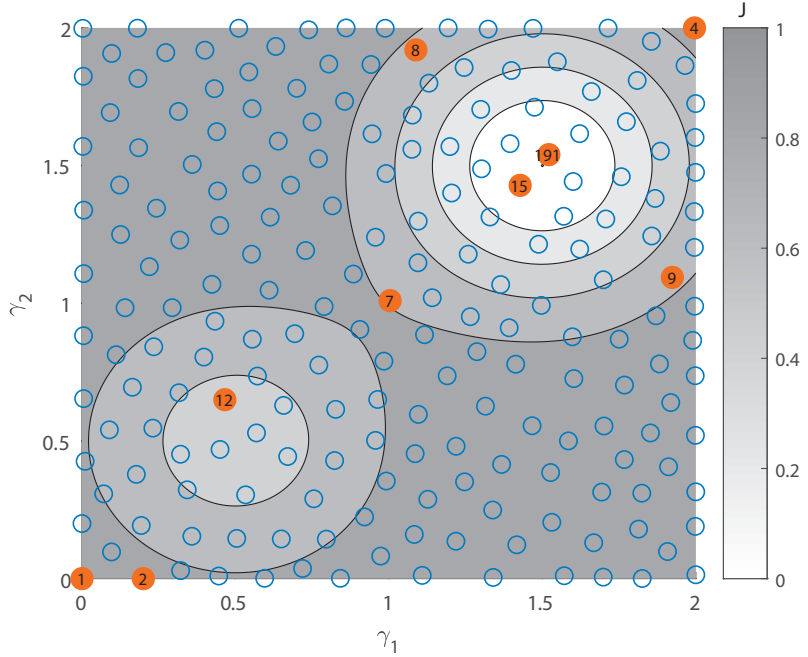


FIGURE 9. Same as figure 7, but for Latin Hypercube Sampling of figure 8.

A more common approach to avoid descending into a suboptimal minimum is ‘random restart or shotgun hill climbing’ (Russell & Norvig 2016), where ‘climbing’ refers to a maximization problem. Here, the gradient search method (here: downhill simplex) is repeatedly started with random initial values. Note that for  $O(10)$  local minima at least  $O(10)$  simplex searches with ideally placed initial conditions need to be performed to assess the terrain. The proposed explorative downhill simplex search requires a number of evaluations corresponding to one additional simplex search at worst: The number of simplex and LHS iterations are the same but the simplex algorithm may require (many) more than one function evaluation. Hence, the explorative gradient search increases the computation cost by at maximum a factor 2 while profiting the effective exploitation of a gradient search. The explorative gradient search has a stochastic explorative component but is distinctly different from *stochastic gradient methods*, like Rechenberg’s evolutionary strategy (Rechenberg 1973) or particle-swarm optimization (Kennedy 2017). The purpose of stochastic gradient methods is a downhill motion in a high-dimensional parameter space in which the computation of gradients constitutes a challenge. We refer to the exquisite optimization textbook by Wahde (2008) for other related methods.

The no-free-lunch theorem reminds us that there exists no optimal algorithm for unspecified data. For any set of algorithms one can find data favourable to any of the algorithms. We assume that the landscape is reasonably smooth with with a couple of minima.

### 3.4. Computational accelerators

The choice of the initial condition for RANS affects the convergence time for the steady solution. The first simulation of an optimization starts with the unforced flow as initial condition. The next iterations exploit the existence of a deterministic mapping from actuation parameters  $\mathbf{b}$  to the corresponding averaged velocity field  $\mathbf{u}(\mathbf{x})$ . The initial

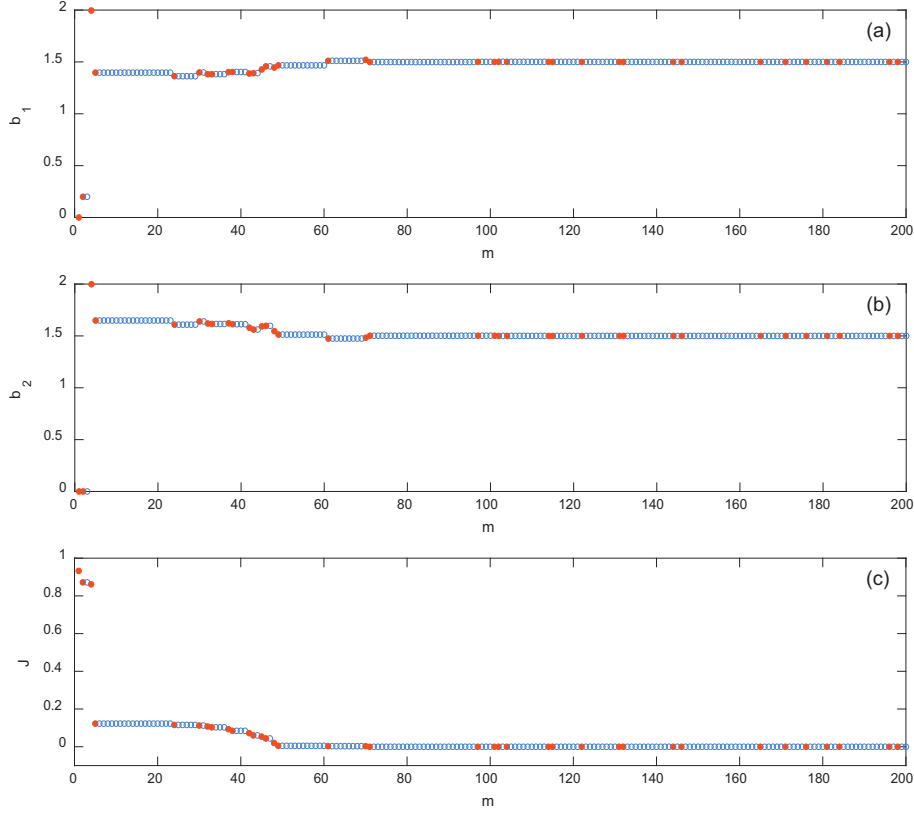


FIGURE 10. Same as figure 6, but for the explorative gradient search.

condition of the  $m$ th simulation is obtained with the 1-nearest-neighbour approach: The velocity field associated with the closest hitherto computed actuation vector is taken as initial condition for the RANS simulation. This simple choice of initial condition saves about 60% CPU time in reduced convergence time.

Another 30% reduction of the CPU time is achieved by avoiding RANS computations with very similar actuations. This is achieved by a quantization of the  $\mathbf{b}$  vector: The actuation velocities are quantized with respect to integral m/s values. This corresponds to increments of  $U_\infty/30$  with  $U_\infty = 30$ m/s. All actuation vectors are rounded with respect to this quantization. If the optimization algorithm yields a rounded actuation vector which has already been investigated, the drag is taken from the corresponding simulation and no new RANS simulation is performed. Similarly, the angles are discretized into integral degrees.

#### 4. Formulation of optimization problem based on streamwise blowing at the top edge

The formulation and constraints of the optimization problem is motivated by the drag reduction results from the top actuator blowing in streamwise direction. Figure 12 shows the drag coefficient in dependency of streamwise blowing velocity, all other actuators being off. The blowing velocity varies in increments of 5 m/s from 0 m/s to 60 m/s, i.e. reaches twice the oncoming velocity.

The drag coefficient is quickly reduced by modest blowing, has a shallow minimum

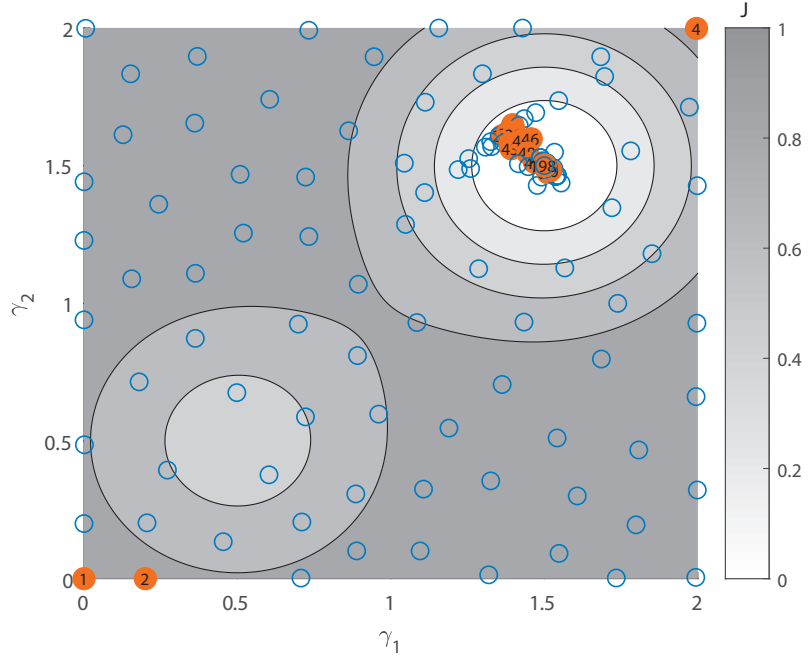


FIGURE 11. Same as figure 7, but for the explorative gradient search displayed in figure 6.

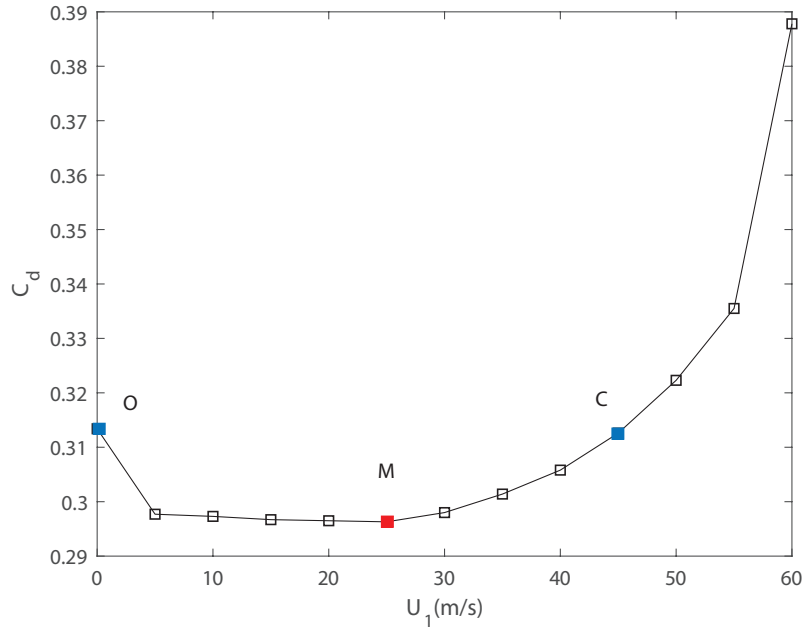


FIGURE 12. Drag coefficient as a function of the blowing velocity  $U_1$  of the streamwise-oriented top actuator. Here, 'O' marks the drag without forcing, 'M' the best actuation, and 'C' the smallest actuation with worse drag than for unforced flow.

near the actuation velocity  $U_{b1} = 25$  m/s before quickly increasing with more intense blowing. This optimal value corresponds to 5/6 of the oncoming velocity. The best drag reduction is 5% with respect to the unforced flow  $C_d = 0.3134$ . Near  $U_1 = 45$  m/s, the drag rapidly rises beyond the unforced value.

This behaviour motivates the choice of actuation parameters. The first five actuation parameters are normalized jet velocities  $b_i = U_i/U_{b1}$ ,  $i = 1, \dots, 5$  introduced in § 2.1. Thus,  $b_1 = 1$  corresponds to minimal drag with a single streamwise-oriented top actuator. All  $b_i$  are capped by 2:  $b_i \in [0, 2]$ ,  $i = 1, \dots, 5$ . At  $b_1 = 1.8$ , point ‘C’ in figure 12, actuation yields already drag increase. The first vertex of the amoeba of the downhill simplex search is put at  $b_1 = b_2 = b_3 = b_4 = b_5 = 1.8$ . From figure 12, we expect a drag minimum at lower values, hence the next five vertices test the value 1.6, e.g.  $(b_1, b_2, \dots, b_5) = (1.8 - 0.2\delta_{1,m-1}, 1.8 - 0.2\delta_{2,m-1}, \dots, 1.8 - 0.2\delta_{5,m-1})$  for  $m = 2, \dots, 6$ . If excluded out-of-domain parameters  $b_i \geq 2$  would yield a maximum drag reduction, the downhill simplex algorithm can be expected to move to the outer border of the actuation domain, thus indicating too restrictive constraints. We refrain from starting already with a much larger actuation domain, as the exploration with LHS and the proposed explorative gradient search will consistently test too many large velocities. An increase of the upper velocity bound by a factor 2, for instance, implies that only  $2^{-5}$  or around 3% of uniformly distributed sampling points are in the original domain and 97% of the samples are outside.

The next five parameters characterize the deflection of the actuator velocity with respect to the streamwise direction (see § 2.1),  $b_{i+5} = \theta_i/(\pi/2)$ ,  $i = 1 \dots, 5$ , and are normalized with  $90^\circ$ . Now all  $b_i$ ,  $i = 1, \dots, 10$  span an interval of width 2, except for the more limited deflection  $b_6$  of the top actuator. Summarizing, the domain for the most general actuation reads

$$\Omega := \left\{ \mathbf{b} \in \mathcal{R}^{10} : \begin{array}{ll} b_i \in [0, 2] & \text{for } i = 1, \dots, 5 \\ b_i \in [-35/90, 1] & \text{for } i = 6 \\ b_i \in [-1, 1] & \text{for } i = 7, \dots, 10 \end{array} \right\}. \quad (4.1)$$

The choice of  $\mathbf{b}$  as symbol shall remind about the control  $B$ -matrix in control theory and is consistent with many earlier publications of the authors, e.g. the review article by Brunton & Noack (2015).

## 5. Optimization of the streamwise trailing edge actuation

The drag of the Ahmed body is optimized with streamwise blowing from the five slot actuators. We apply a simplex downhill search, Latin hypercube sampling and the explorative gradient search of § 5.1, § 5.2 and § 5.3, respectively.

### 5.1. Downhill simplex algorithm

Following § 4, the downhill simplex algorithm is centered around  $b_i = 1.8$ ,  $i = 1, \dots, 5$  as first vertex and explores a lower actuation  $b_{m-1} = 1.6$  in all directions for vertices  $m = 2, \dots, 6$ . Table 2 shows the values of the individuals and corresponding cost. All vertices have a larger drag than for the unforced benchmark  $C_d = 0.3134$ . And all vertices with  $b_i = 1.6$  are associated with a smaller drag indicating a downhill slide to small actuation values consistent with the expectations from § 4.

Figure 13 shows the evolution of the downhill simplex algorithm with 200 RANS simulations. Like in § 3, solid red circles mark newly found optima while open blue circles record the best actuation so far. The drag quickly descends after staying shortly on a plateau at  $m \approx 20$ . From there on, the descend becomes gradual. The optimal

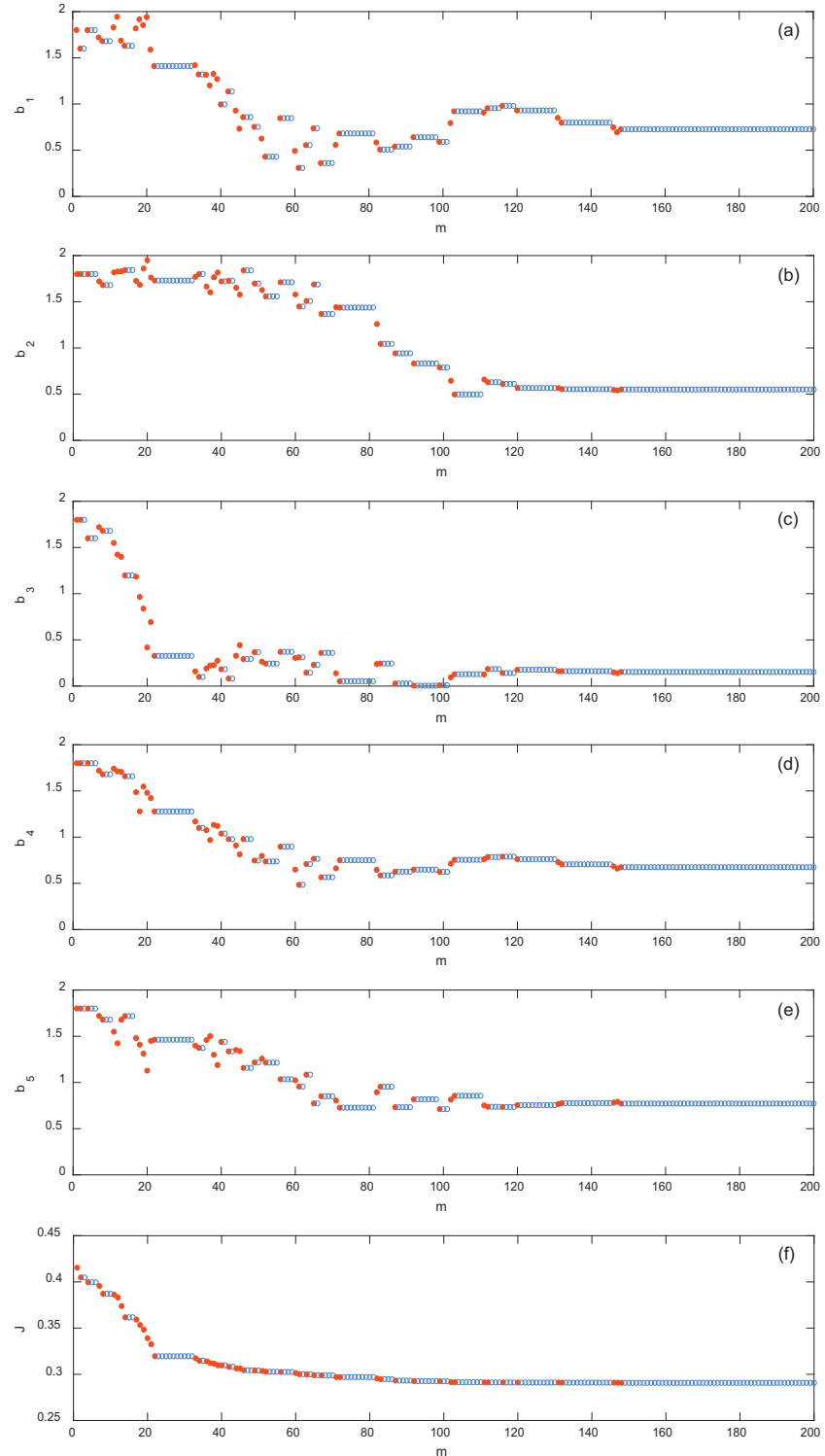


FIGURE 13. Optimization of the streamwise trailing edge actuation during a downhill simplex search. The actuation parameters and cost is visualized like in figure 6.  $m$  counts the RANS simulation calls for drag computation.

$m$	$b_1$	$b_2$	$b_3$	$b_4$	$b_5$	$J$
1	1.8	1.8	1.8	1.8	1.8	0.4153
2	1.6	1.8	1.8	1.8	1.8	0.4048
3	1.8	1.6	1.8	1.8	1.8	0.4109
4	1.8	1.8	1.6	1.8	1.8	0.3996
5	1.8	1.8	1.8	1.6	1.8	0.4075
6	1.8	1.8	1.8	1.8	1.6	0.4040

TABLE 2. Initial simplex ( $m = 1, \dots, 6$ ) for the five-dimensional downhill simplex optimization.  $b_i$  are the normalized actuation velocities and  $J$  corresponds to the drag coefficient.

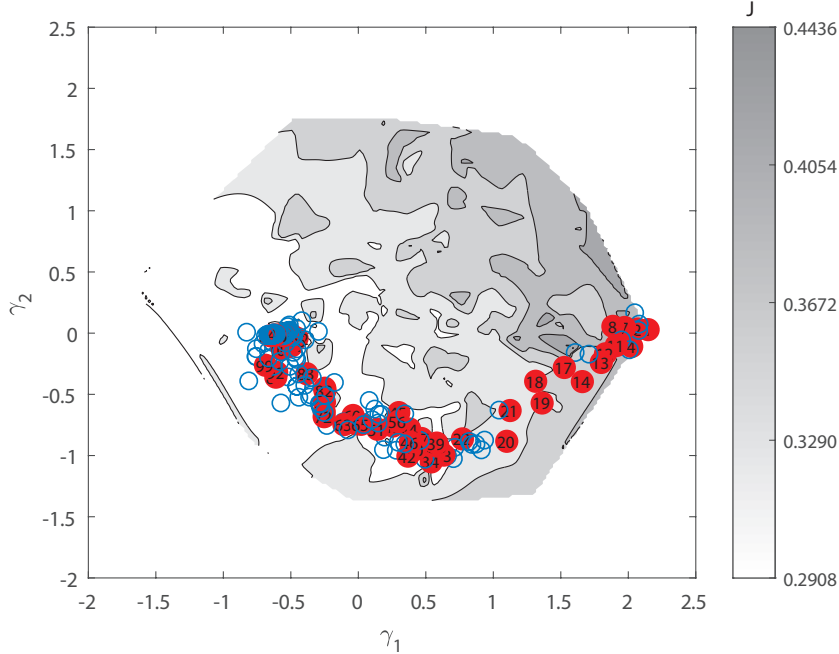


FIGURE 14. Proximity map of the streamwise trailing edge actuation during downhill simplex search. The contour plot corresponds to the interpolated cost function (drag coefficient) from all RANS simulations of this section. As in figure 13, solid red circles mark newly find optima while open blue circles mark unsuccessful explorations of cost functions.

drag  $J = 0.2908$  is reached with the 148th RANS simulation and corresponds to 7% drag reduction. The optimal actuation reads  $b_1 = 0.7264$ ,  $b_2 = 0.5508$ ,  $b_3 = 0.1533$ ,  $b_4 = 0.6746$ ,  $b_5 = 0.7716$ . While the middle horizontal jet has small amplitude, the other actuation velocities on the four edges of the Ahmed body are 55% to 77% of the optimal value achieved with single actuator.

Figure 14 illustrates the downhill search in a control landscape  $J(\gamma_1, \gamma_2)$  described in § 3. Here  $(\gamma_1, \gamma_2)$  feature vectors defining a proximity map of the five-dimensional actuation parameters  $(b_1, \dots, b_5)$ . This landscape indicates a complex topology of the five-dimensional actuation space by many local maxima and minima in the feature plane. This complexity may explain why most simplex steps did not yield a better cost. The feature coordinate  $\gamma_1, \gamma_2$  arise from a kinematic optimization process and have no inherent

meaning. The simplex algorithm is seen to crawl from right  $\gamma \approx (2, 0)$  to the assumingly global minimum at  $\gamma \approx (-0.6, 0)$  through an elongated curved valley.

### 5.2. Latin hypercube sampling

Figure 15 shows the slow learning process associated with Latin hypercube sampling (LHS) starting with the simplex reference point  $b_1 = \dots = b_5 = 1.8$ . Apparently the optimization is ineffective. Only 4 new optima are successively obtained in 200 RANS simulations. The remaining simulations yield worse drags than the best discovered before. At the 162th RANS simulation, the best drag coefficient of  $C_d = 0.2928$ , with  $b_1 = 0.8366$ ,  $b_2 = 0.8302$ ,  $b_3 = 0.0269$ ,  $b_4 = 0.3421$  and  $b_5 = 0.6092$ . This corresponds to 5% reduction like the one-dimensional top actuator  $b_1 = 1$ ,  $b_2 = b_3 = b_4 = b_5 = 0$ . The corresponding LHS actuation parameters read  $b_1 = 0.0994$ ,  $b_2 = 0.9587$ ,  $b_3 = 0.1276$ ,  $b_4 = 0.0289$  and  $b_5 = 1.0393$ . Intriguingly, only the upper side and bottom actuator have  $b_i$  amplitudes near unity while remaining parameters are less than 13% of the one-dimensional optimum. These results show that near optimal drag reductions can be achieved with quite different actuators. Moreover, individual actuation effects are far from additive. Otherwise, the almost complimentary LHS optimum for actuators 2–5 and the one-dimensional optimum of § 4 should yield 10% reduction with  $b_1 \approx 1$ ,  $b_2 \approx 1$ ,  $b_3 \approx 0.13$ ,  $b_4 \approx 1$  and  $b_5 \approx 1$ .

Figure 16 shows the LHS in the control landscape. In the first iteration, LHS jumps to the opposite site of domain and finds better drag. The next successive two improvements are in a good terrain but the optimum at  $m = 162$  is still far from the assumingly global minimum at  $\gamma = (-0.6, 0)$  (see figure 14). The exploratory steps uniformly cover the whole range of feature vectors.

### 5.3. Explorative gradient search

From figure 17, the explorative gradient search is seen to converge much faster than the downhill simplex algorithm. The best actuation is found at the 65th RANS simulation yielding the same drag coefficient  $C_d = 0.2908$  of the downhill simplex algorithm with only slightly different actuation parameters  $b_1 = 0.6647$ ,  $b_2 = 0.4929$ ,  $b_3 = 0.1794$ ,  $b_4 = 0.7467$ ,  $b_5 = 0.7101$ .

The fast convergence of the explorative gradient search is initially surprising since up to 50% of the steps are for explorative purposes, i.e. shall identify distant minima. However, the control landscape in figure 18 reveals how the explorative LHS steps help the algorithm to prevent the long and painful march through the long and curved valley. The proposed new algorithm operates like a visionary mountain climber, who performs not only local uphill steps but sends drones to the remotest location to find better mountains and terrains.

## 6. Optimization of the directed trailing edge actuation

In this section, the actuation space is enlarged by the jet directions of all slot actuators. The jets may now be directed inwards or outwards as discussed in § 2.1. The actuation optimization for drag reduction is performed with explorative gradient search (§ 6.1). The unforced and three actuated Ahmed body wakes are investigated in § 6.2.

### 6.1. Explorative gradient search

We employ the explorative gradient search as best performing method of § 5 for the 10-dimensional actuation optimization problem. The search is accelerated by starting with a simplex centered around the optimal actuation of the five-dimensional problem. The first vertex of table 3 contains this optimal solution. The cost is 4% lower than the previous

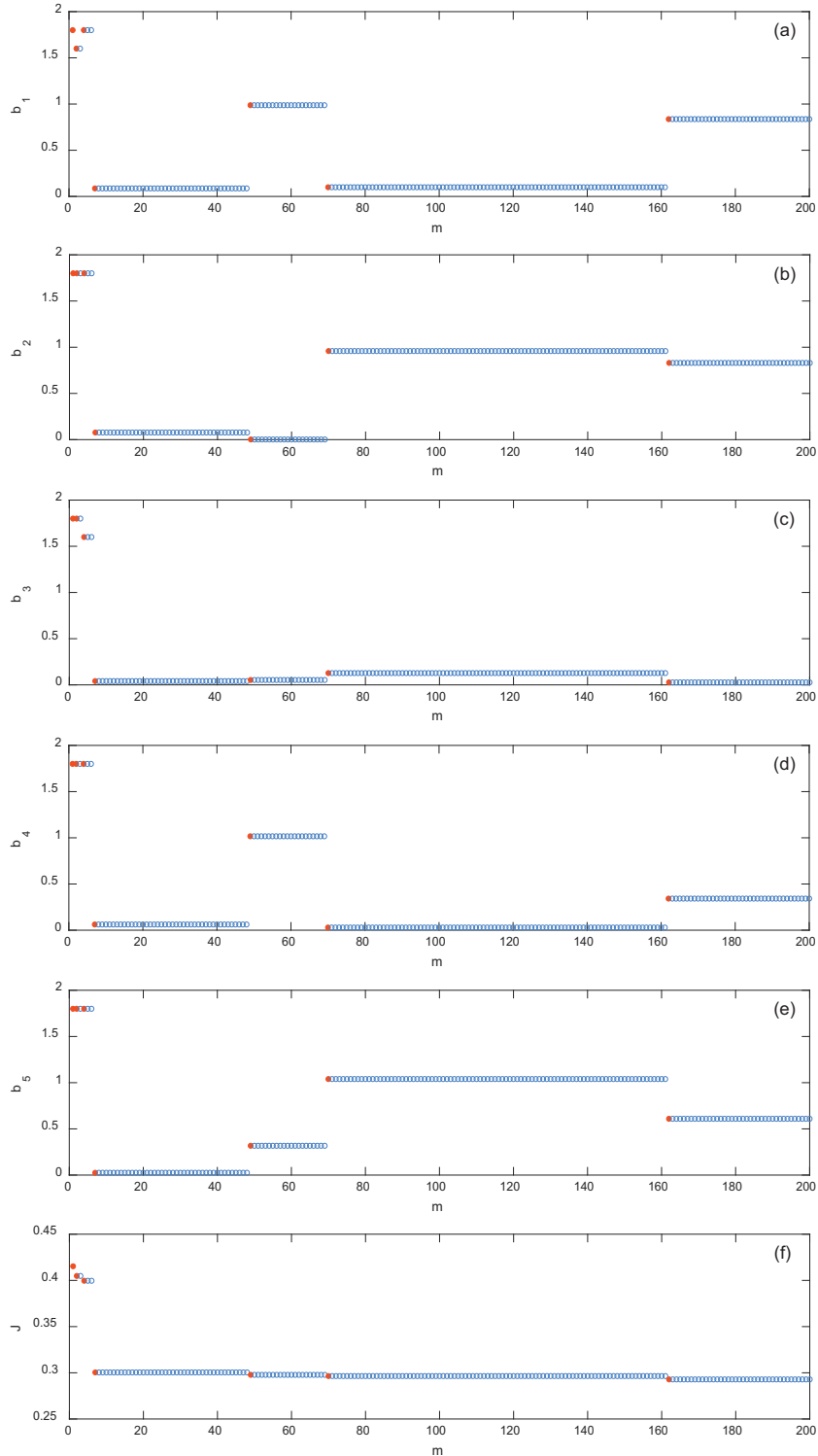


FIGURE 15. Same as figure 13 but for Latin hypercube sampling (streamwise trailing edge actuation).

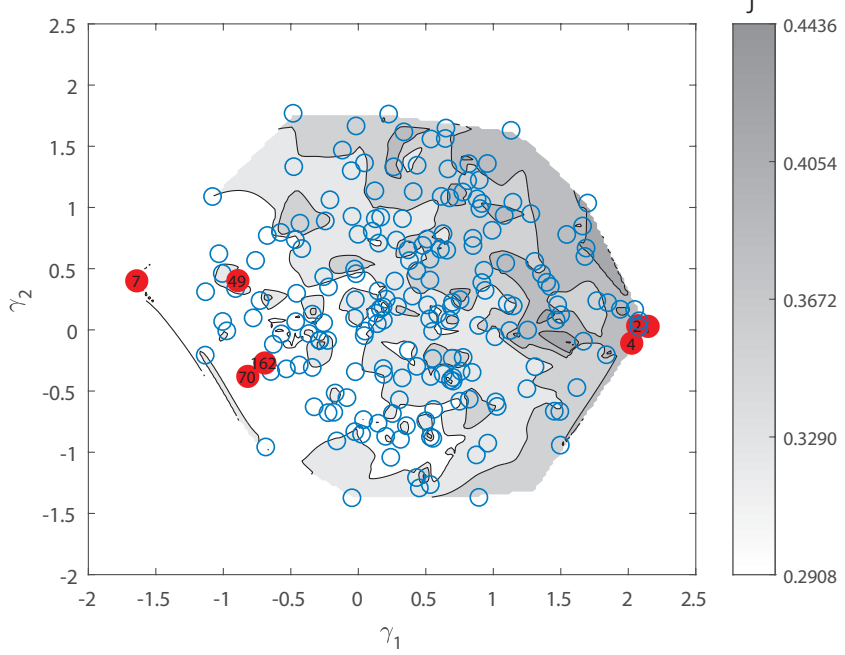


FIGURE 16. Same as figure 14 but for Latin hypercube sampling (streamwise trailing edge actuation).

$m$	$b_1$	$b_2$	$b_3$	$b_4$	$b_5$	$b_6$	$b_7$	$b_8$	$b_9$	$b_{10}$	$J$
1	0.6647	0.4929	0.1794	0.7467	0.7101	0	0	0	0	0	0.2895
2	0.6647	0	0	0	0	1/2	0	0	0	0	0.3268
3	0	0.4929	0	0	0	0	1/2	0	0	0	0.3226
4	0	0	0.1794	0	0	0	0	1/2	0	0	0.3168
5	0	0	0	0.7467	0	0	0	0	1/2	0	0.3476
6	0	0	0	0	0.7101	0	0	0	0	1/2	0.3060
7	0.6647	0	0	0	0	-35/90	0	0	0	0	0.3091
8	0	0.4929	0	0	0	0	-1/2	0	0	0	0.3085
9	0	0	0.1794	0	0	0	0	-1/2	0	0	0.3187
10	0	0	0	0.7467	0	0	0	0	-1/2	0	0.3001
11	0	0	0	0	0.7101	0	0	0	0	-1/2	0.3354

TABLE 3. Initial individuals in the optimization of the directed trailing edge actuation.  $b_i$ ,  $i = 1, 2, 3, 4, 5$  represent the actuation amplitudes  $U_i$  of the  $i$ th actuator.  $b_i$ ,  $i = 6, 7, 8, 9, 10$  denotes the actuation angle  $\theta_i$  of the  $(i - 5)$ th actuator.  $J$  is the drag coefficient.

section as the RANS integration for the first flow is not fully converged. The next five vertices represent isolated actuations at the optimal value but directed 45° outwards for the side edges and upwards for the middle horizontal actuator. The corresponding drag values are larger. The next five vertices deflect the jets in opposite direction by 45° or the maximum 35° of the top actuator, giving rise smaller drag than the previous deflection. The drag of middle horizontal actuator remains close to the unforced benchmark because the jet velocity is small.

Figure 19 illustrates the convergence of the explorative gradient search. After 289

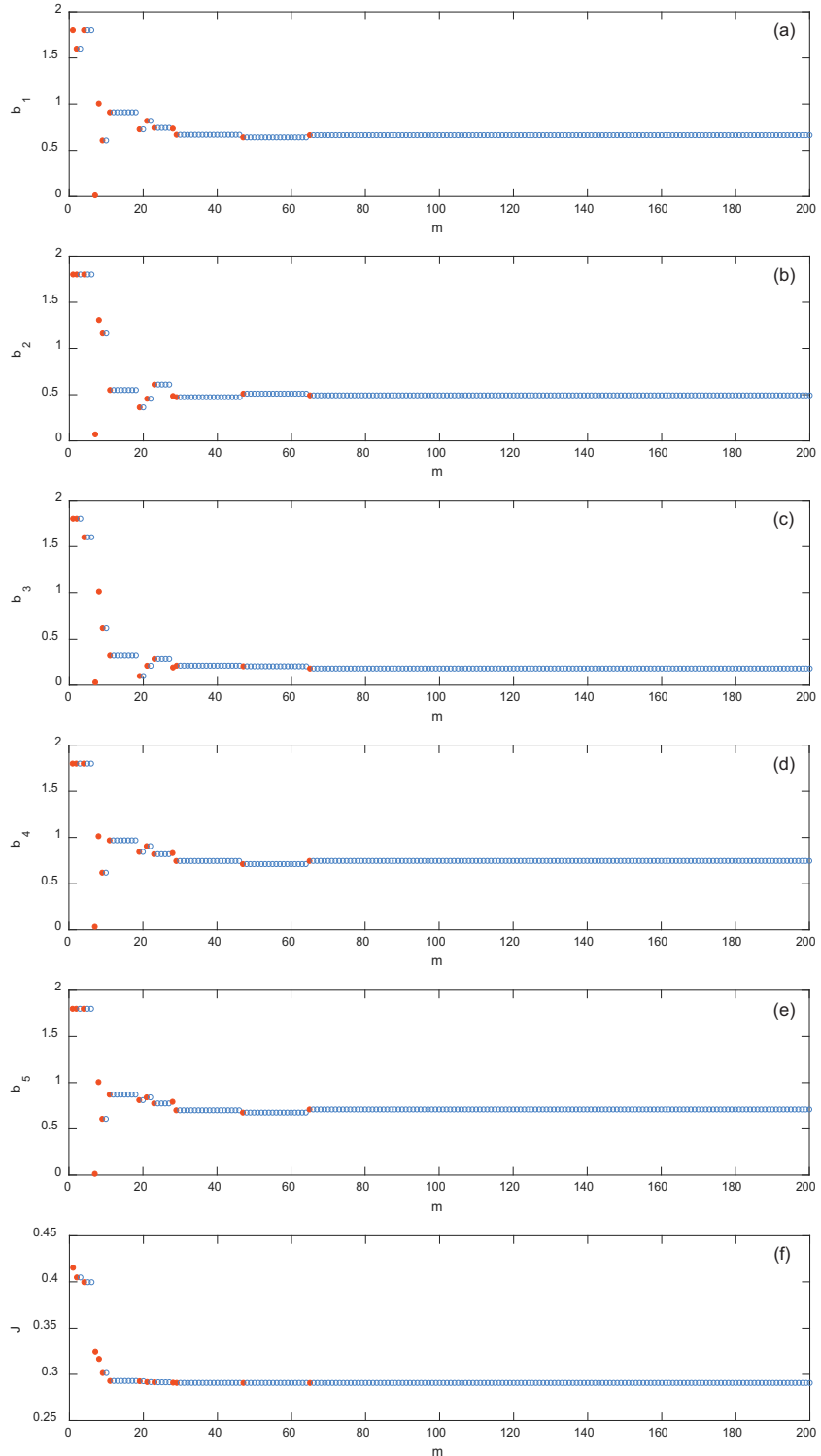


FIGURE 17. Same as figure 13 but for the explorative gradient search (streamwise trailing edge actuation).

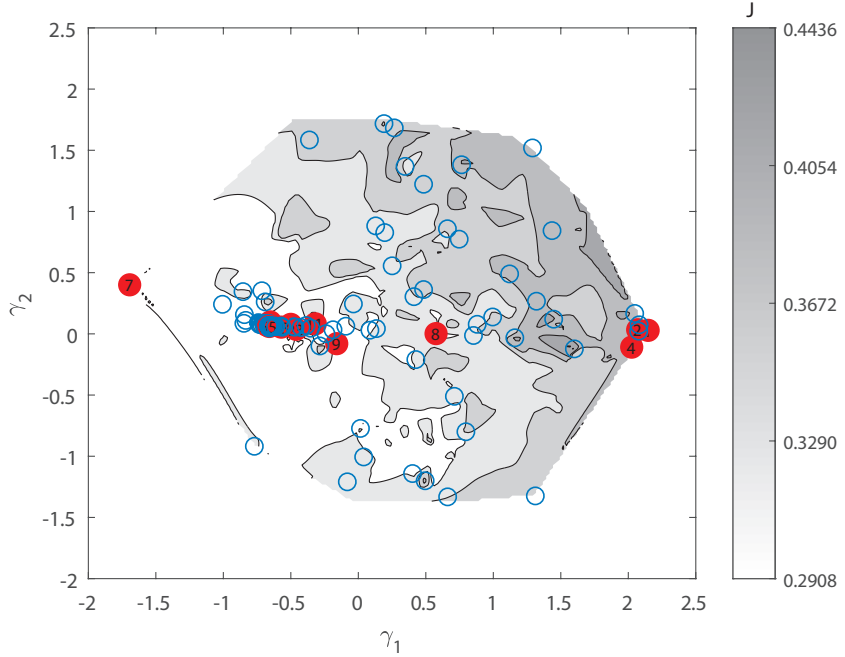


FIGURE 18. Same as figure 14 but for the explorative gradient search (streamwise trailing edge actuation).

RANS simulations, a drag coefficient of 0.2586 is achieved corresponding to a 17% drag reduction. The optimal actuation values read  $b_1 = 0.8611$ ,  $b_2 = 0.9856$ ,  $b_3 = 0.0726$ ,  $b_4 = 1.0089$ ,  $b_5 = 0.8981$ ,  $b_6 = -0.3000$  corresponding to  $\theta_1 = -27^\circ$ ,  $b_7 = -0.4666$  ( $\theta_2 = -42^\circ$ ),  $b_8 = 0.7444$  ( $\theta_3 = 67^\circ$ ),  $b_9 = -0.4888$  ( $\theta_3 = -44^\circ$ ), and  $b_{10} = 0.2444$  ( $\theta_3 = -22^\circ$ ). All outer actuators have velocity amplitudes near unity and are directed inwards, i.e. emulate Coanda blowing. The third middle actuator blows upward with low amplitude. The strong inward blowing seems to be related to the additional 10% drag reduction as compared to the 7% of streamwise actuation.

Figure 20 shows the search process in a proximity map. It should be noted that this control landscape is based on data in a ten-dimensional actuation space and hence different from the 5-dimensional space in § 5. The algorithm quickly descends in the valley while many exploration steps probe suboptimal terrain. One reason for this quick landing in good terrain is the chosen initial simplex around the optimized actuation in the five-dimensional subspace.

### 6.2. Discussion of streamwise and directed jet actuators

In the following, the physical structures associated with the optimized one-, five- and ten-dimensional actuation are discussed. Evidently, more degrees of freedom are associated with more opportunities for drag reduction. Expectedly, the drag reduces by 5% to 7% to 17% as the dimension of the actuation parameters increase from 1 to 5 to 10, respectively. Intriguingly, the increase of drag reduction from the optimized top actuator to the best 5 streamwise actuators is only 2%. For the square-back Ahmed body, Barros (2015) experimentally observed that the individual drag reductions from the streamwise blowing actuators on the four trailing edges roughly add up to the total drag reduction of 10% with all actuators on. This additivity of actuation effects is not corroborated for the

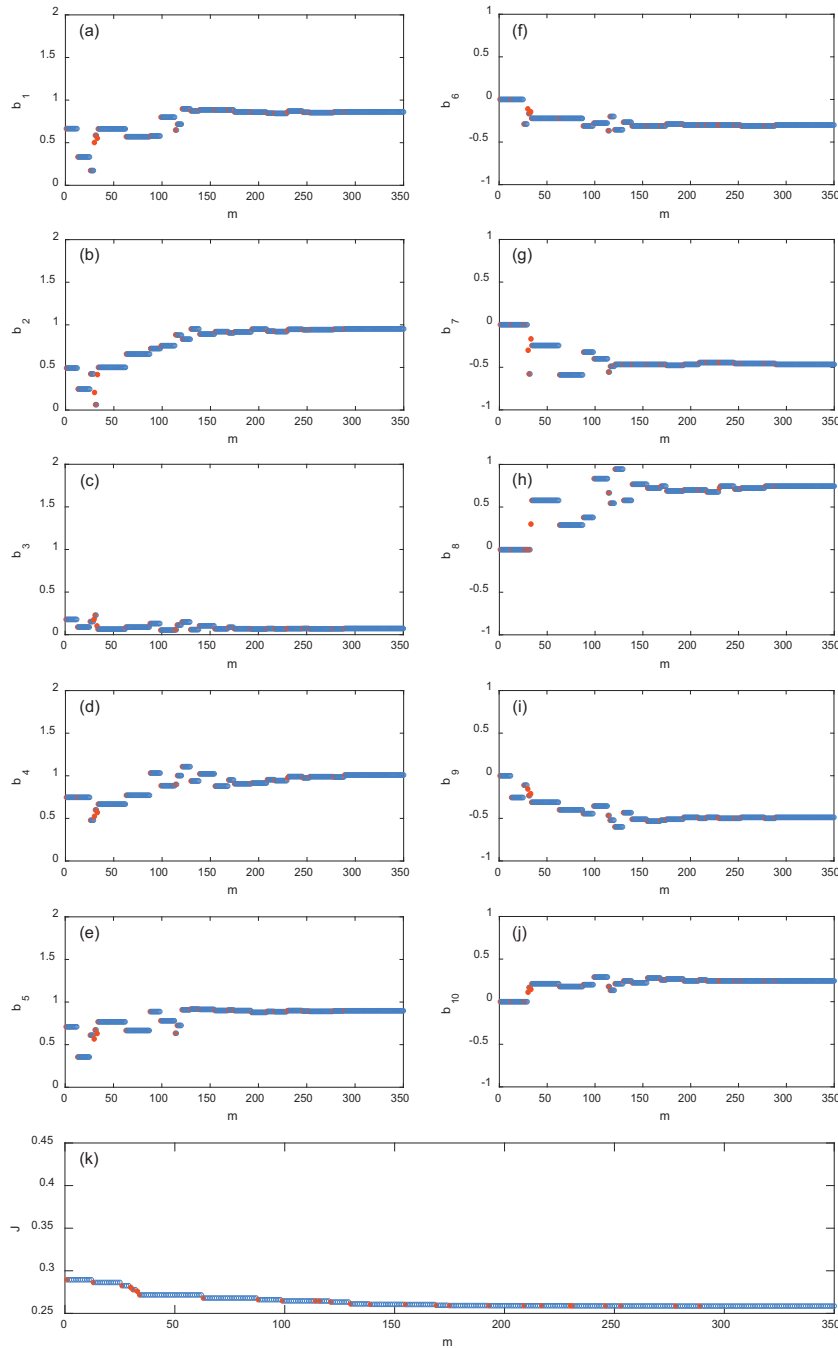


FIGURE 19. Optimization of the directed trailing edge actuation during explorative gradient search.  $J$ : cost function (drag coefficient);  $m$  the number of RANS calls by the algorithm. Red solid circles and blue open circles have the same meaning as in previous convergence plots. The actuation includes the amplitudes: (a)  $b_1$ , (b)  $b_2$ , (c)  $b_3$ , (d)  $b_4$ , (e)  $b_5$ , and the angles: (f)  $b_6$ , (g)  $b_7$ , (h)  $b_8$ , (i)  $b_9$ , (j)  $b_{10}$ .

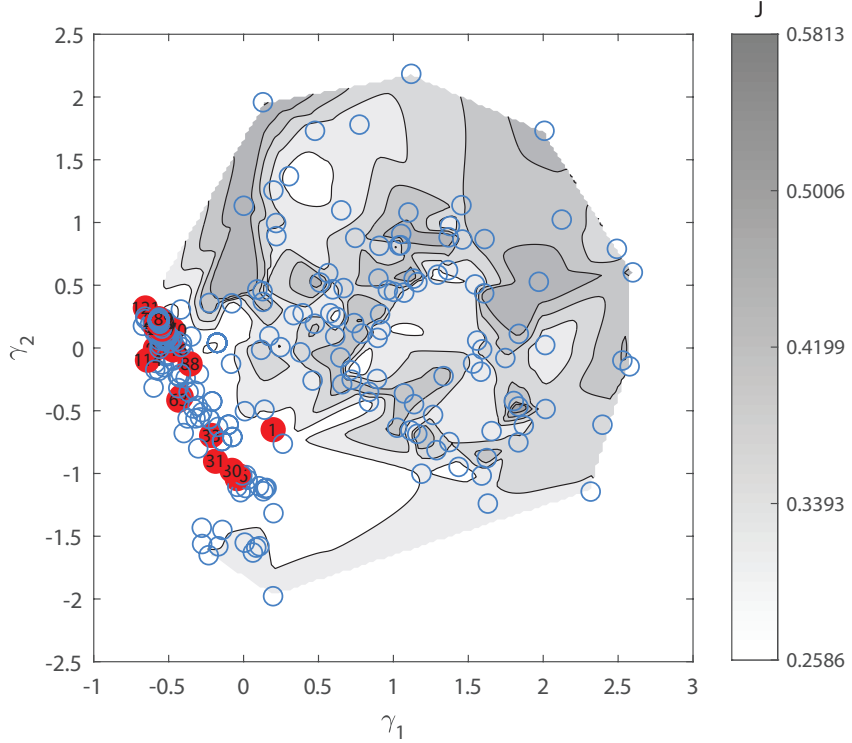


FIGURE 20. Proximity map of the directed trailing edge actuation during explorative gradient search. The contour indicates the interpolated cost function (drag coefficient). Red solid circles and blue open circles have the same meaning as in previous control landscapes.

Case	Drag reduction	Actuation parameters				
		Top	Upper side	Middle	Lower side	Bottom
A)	0%	—	—	—	—	—
B)	5%	$b_1 = 1$	$b_2 = 0$	$b_3 = 0$	$b_4 = 0$	$b_5 = 0$
C)	7%	$b_1 = 0.6647$	$b_2 = 0.4929$	$b_3 = 0.1794$	$b_4 = 0.7467$	$b_5 = 0.7101$
D)	17%	$b_1 = 0.8611$ $\theta_1 = -27^\circ$	$b_2 = 0.9856$ $\theta_2 = -42^\circ$	$b_3 = 0.0726$ $\theta_3 = 67^\circ$	$b_4 = 1.0089$ $\theta_4 = -44^\circ$	$b_5 = 0.8981$ $\theta_5 = -22^\circ$

TABLE 4. Investigated optimized actuators in comparison to the unforced benchmark. The table shows the achieved drag reduction and corresponding actuation parameters for A) the unforced benchmark, and for the optimized B) top streamwise actuator, C) all streamwise actuators, D) all deflected actuators.

slanted low-drag Ahmed body. Intriguingly, the inward deflection of the jet-slot actuators substantially decreases drag by 10%. This additional drag reduction of 10% has also been observed for the square-back Ahmed body when the horizontal jets were deflected inward with Coanda surfaces on all four edges (Barros *et al.* 2016). Improved drag reduction with inward as opposed to tangential blowing was also observed for the 35° high-drag Ahmed body (Zhang *et al.* 2018) and the square back version Schmidt *et al.* (2015).

Table 4 summarizes the discussed flows, associated drag reduction and actuation parameters. For brevity, we refer to flows with no, one-dimensional, five-dimensional and

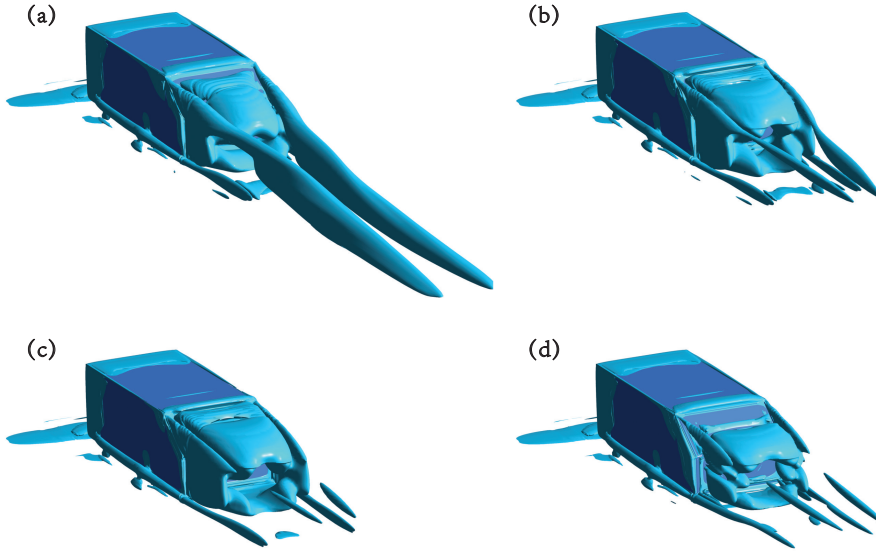


FIGURE 21. Okubo-Weiss parameter  $Q$  of flow. *a)* without control and under *b)* 1D, *c)* 5D and *d)* 10D control respectively, where  $Q = 15000/s^2$ .

ten-dimensional actuation spaces as case A, B, C and D, respectively. The actuation energy may be conservatively estimated by the energy flux through all jet actuators:  $\sum_{i=1}^5 \int dA_i \rho U_i^3 / 2$ . Here, the actuation jet fluid is assumed to be accelerated from 0 to the actuation jet velocity  $U_i$  and then deflected after the outlet, e.g. via a Coanda surface. In this case, the actuation energy of cases *B*, *C* and *D* would correspond to 3.2%, 3.0% and 7.9% of the parasitic drag power, respectively. This expenditure is significantly less than the saved drag power. The ratio from saved drag power to actuation energy is comparable for a truck model where steady Coanda blowing with 7% energy expenditure yields a 25% drag reduction (Pfeiffer & King 2014). This estimate should not be taken too literally as actuation energy strongly depends on the realization of the actuator. It would be less, more precisely  $\sum_{i=1}^5 \int dA_i \rho \cos(\theta_i) U_i^3 / 2$ , when the actuation jet fluid leaves the Ahmed body through a slot directed with the jet velocity and can be expected much less when this fluid is taken from the oncoming flow, e.g. from the front of the Ahmed body.

Figure 21 displays iso-surfaces for the same Okubo-Weiss parameter value  $Q$  for all four cases. The unforced case A (figure 21*a*) shows a pronounced C-pillar vortices extending far into the wake. Under streamwise top actuation (case B, figure 21*b*), the C-pillar vortices significantly shorten. The next change with all streamwise actuators optimized (case C) is modest consistent with the small additional drag decrease. The C-pillar vortices are slightly more shortened (see figure 21*c*). The inward deflection of the actuation (case D) is associated with aerodynamic boat tailing as displayed in figure 21*d*. The separation from the slanted window is significantly delayed and the sidewise separation is vectored inward.

This actuation effect on the C-pillar vortices is corroborated by the streamwise vorticity contours in a transverse plane on body height downstream ( $x/H = 1$ ). Figure 22 shows this averaged vorticity component for case A–D in subfigure *a*–*d*, respectively. The extend of the C-pillar vortices clearly shrink with increasing drag reduction.

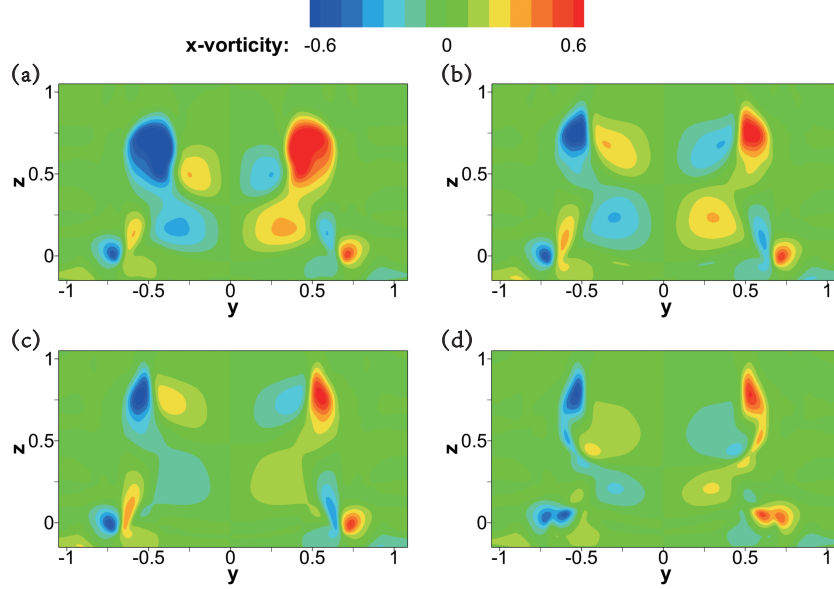


FIGURE 22. Streamwise vorticity component in near-wake plane  $x/H = 1$ . a) without forcing and under b) 1D, c) 5D and d) 10D control respectively.

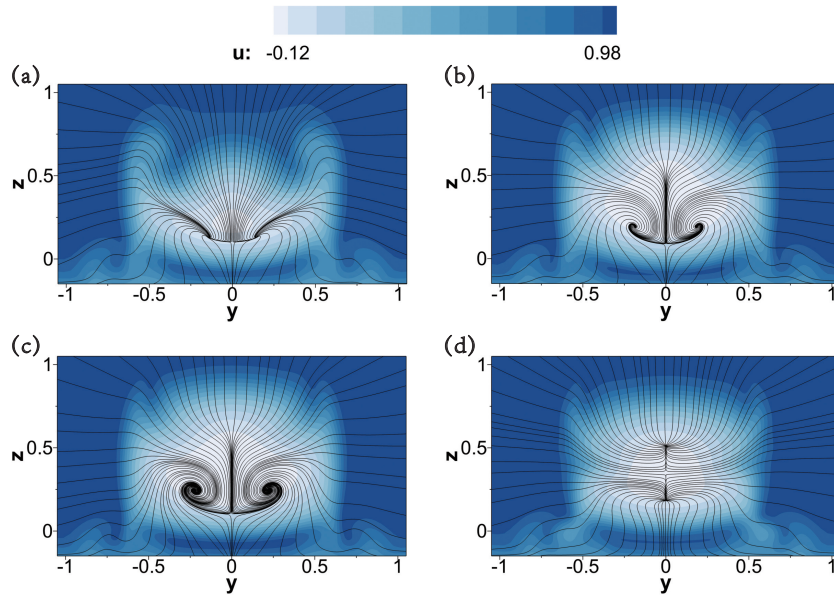


FIGURE 23. Streamwise velocity component in the near-wake transversal plane  $x/H = 1$  and streamlines from the in-plane velocity components. a) without forcing and under b) 1D, c) 5D and d) 10D control respectively.

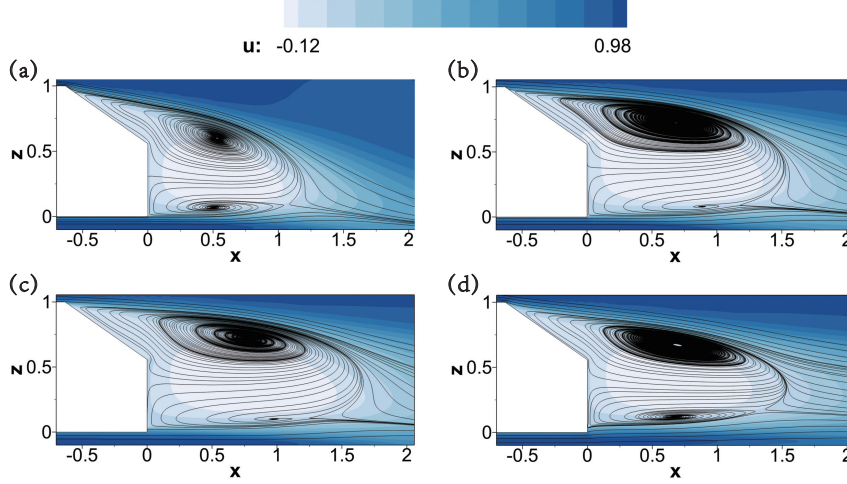


FIGURE 24. Streamwise velocity component in the symmetry plane  $y = 0$  and streamlines from the in-plane velocity components. a) without forcing and under b) 1D, c) 5D and d) 10D control respectively.

Figure 23 shows the streamwise velocity component and streamlines of the transversal velocity in the same plane for the same cases. Cases B and C feature a larger region of upstream flow while case D has a narrowed regions of backflow. From these visualizations, one may speculate that the drag reduction from streamwise actuation (cases B and C) is due to a wake elongation towards the Kirchhoff solution while the inward directed actuation (case D) is associated with drag reduction from aerodynamic boat-tailing.

This hypothesis about different mechanisms of drag reduction is corroborated from the streamlines in the symmetry plane  $y = 0$  in figure 24. The tangential blowing (see subfigures b, c) leads to an elongated fuller wake as compared to the unforced benchmark (subfigure a). The top shear-layer is oriented more horizontal under streamwise actuation—consistent with the Kirchhoff wake solution. The inward-directed actuation (see subfigure d) also elongates the wake but gives rise to a more streamlined shape. The top and bottom shear-layers are vectored inward.

The drag reduction can more directly be inferred from the  $C_p$  distribution of the rearward windows in figure 25. The 5% drag reduction in subfigure b) for case B is associated with a pressure increase of the vertical surface. The additional 2% drag decrease for case C in subfigure c is accompanied by an increase over vertical and slanted surface. The aerodynamic boat-tailing of case D with 17% drag reduction alleviates significantly the pressures on both surfaces.

## 7. Conclusions

This numerical study proposes a novel optimization approach for active bluff-body control exploiting local gradients with a downhill simplex algorithm and exploring new better minima with Latin hypercube sampling. The computational load for the exploration is less than for the simplex iterations. This compares favourably with a shotgun downhill optimization typically requiring dozens of converged downhill simplex applications.

This approach named *explorative gradient search (EGS)* minimizes the drag of an  $35^\circ$  slanted Ahmed body at Reynolds number  $Re_H = 1.9 \times 10^5$  with independent steady

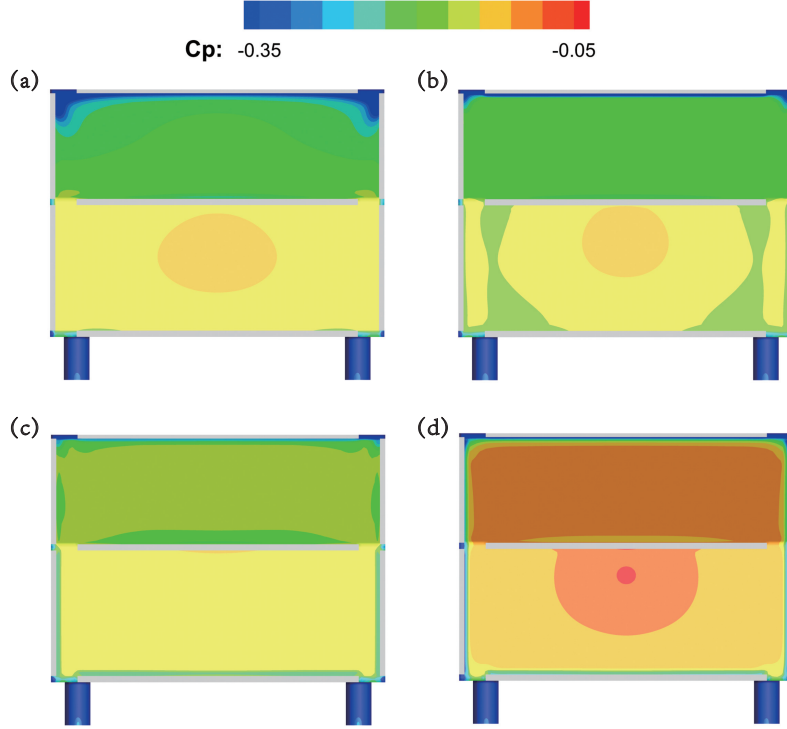


FIGURE 25. Pressure coefficient on the slant and vertical base of flow. *a)* without forcing and under *b)* 1D, *c)* 5D and *d)* 10D control respectively.

blowing at all trailing edges. The 10-dimensional actuation space includes 5 symmetric jet slot actuators or corresponding actuator groups with variable velocity and variable blowing angle. The resulting drag is computed with a Reynolds-Averaged Navier-Stokes (RANS) simulation.

The approach is augmented by auxiliary methods for initial conditions, for accelerated learning and for a control landscape visualization. The initial condition for a RANS simulation with a new actuation is computed by the 1-nearest neighbour method. In other words, the RANS simulation starts with the converged RANS flow of the closest hitherto examined actuation. This cuts the computational cost by 60% as it accelerates RANS convergence. The actuation velocities are quantized to prevent testing of too similar control laws. This optional element reduces the CPU time by roughly 30%. The learning process is illustrated in a control landscape. This landscape depicts the drag in a proximity map—a two-dimensional feature space from the high-dimensional actuation response. Thus, the complexity of the optimization problem can be assessed.

In a analytical example, the explorative gradient search is found to outperform the downhill simplex method converging to suboptimal minimum and a Latin hypercube sampling needing too many iterations. The slanted Ahmed body with 1, 5 and 10 actuation parameters constitutes a more realistic plant for an optimization algorithm. First, only the upper streamwise jet actuator is optimized. This yields drag reduction of 5% with pronounced global minimum for the jet velocity. Second, the drag can be further reduced to 7% with 5 independent streamwise symmetric actuation jets. Intriguingly, the actuation effects of the actuator are far from additive—contrary to the experimental

observation for the square-back Ahmed body Barros (2015). The optimal parameters of a single actuator are not closely indicative for the optimal values of the combined actuator groups. The control landscape depicts a long curved valley with small gradient leading to a single global minimum. Interestingly, the explorative step is not only a security policy for the right minimum. It also helps to accelerate the optimization algorithm by jumping out of the valley to a point closer to the minimum.

A significant further drag reduction of 17% is achieved when, in addition to the jet velocities, also the jet angles are included in the optimization. Intriguingly, all trailing edge jets are deflected inward mimicking the effect of Coanda blowing and leading to fluidic boat tailing. The C-pillar vortices are increasingly weakened with one-, five- and ten-dimensional actuation. Compared with the pressure increase at C-pillar in one- and five-dimensional control, the ten-dimensional control brings a substantial pressure recovery over the entire base. The achieved 17% drag decrease with constant blowing is comparable with the experimental 20% reduction with high-frequency forcing by Bideaux *et al.* (2011); Gilliéron & Kourta (2013).

For the 25° high-drag Ahmed body, (Zhang *et al.* 2018) have achieved 29% drag reduction with steady blowing at all sides, thus significantly outperforming all hitherto existing active flow control studies cited therein. The actuation has only been investigated for few selected actuation values. Hence, even better drag reductions are conceivable. Yet, the unforced high-drag Ahmed body has a significantly higher drag coefficient of 0.361 than the low-drag version and is hence not fully comparable. Their reduced drag coefficient of 0.256 is almost identical with the one of this study.

We expect that our RANS-based active control optimization is widely applicable for virtually all multi-input steady actuators or combinations of passive and active control Bruneau *et al.* (2010). The explorative gradient search mitigates the chances of sliding down a suboptimal minimum at a acceptable cost. The 1-nearest neighbour method for initial condition and the actuation quantization accelerate the simulations and learning processes. And the control landscape provides the topology of the actuation performance, e.g. the number of local minima, nature and shape of valleys, etc.

## Acknowledgements

This work is supported by Shanghai Key Lab of Vehicle Aerodynamics and Vehicle Thermal Management Systems (Grant No.18DZ2273300), by public grants overseen by the French National Research Agency (ANR) ANR-11-IDEX-0003-02 (iCODE Institute project, IDEX Paris-Saclay), and ANR-17-ASTR-0022 (FlowCon), 'ACTIV\_ROAD'.

We have profited from stimulating discussions with Steven Brunton, Siniša Krajnović, Francois Lusseyran, Navid Nayeri, Oliver Paschereit, Luc Pastur, Richard Semaan, Wolfgang Schröder, Bingfu Zhang and Yu Zhou.

## REFERENCES

- AIDER, J.-L., BEAUDOIN, J.-F. & WESFREID, J. E. 2010 Drag and lift reduction of a 3d bluff-body using active vortex generators. *Exp. Fluids* **48**, 771–789.
- BARROS, D. 2015 Wake and drag manipulation of a bluff body using fluidic forcing. PhD thesis, École Nationale Supérieure de Mécanique et d'Aérotechnique, Poitiers, France.
- BARROS, D., BORÉE, J., CADOT, O., SPOHN, A. & NOACK, B. R. 2017 Forcing symmetry exchanges and flow reversals in turbulent wakes. *J. Fluid Mech.* **829**, R1.
- BARROS, D., BORÉE, J., NOACK, B. R., SPOHN, A. & RUIZ, T. 2016 Bluff body drag manipulation using pulsed jets and Coanda effect. *J. Fluid Mech.* **805**, 442–459.

- BEN-HAMOU, E., ARAD, E. & SEIFERT, A. 2007 Generic transport aft-body drag reduction using active flow control. *Flow Turbul. Combust.* **78** (3-4), 365.
- BIDEAUX, E., BOBILLIER, P., FOURNIER, E., GILLIÉRON, P., EL HAJEM, M., CHAMPAGNE, J.-Y., GILLOTTE, P. & KOURTA, A. 2011 Drag reduction by pulsed jets on strongly unstructured wake: towards the square back control. *Int. J. Aerodyn.* **1** (3-4), 282–298.
- BRUNEAU, C.-H., CREUSÉ, E., DEPEYRAS, D., GILLIÉRON, P. & MORTAZAVI, I. 2010 Coupling active and passive techniques to control the flow past the square back Ahmed body. *Comput. & Fluids* **39** (10), 1875–1892.
- BRUNN, A. & NITSCHE, W. 2006 Drag reduction of an ahmed car model by means of active separation control at the rear vehicle slant. In *New Results in Numerical and Experimental Fluid Mechanics V*, pp. 249–256. Springer.
- BRUNTON, S. L. & NOACK, B. R. 2015 Closed-loop turbulence control: Progress and challenges. *Appl. Mech. Rev.* **67** (5), 050801:01–48.
- DEJOAN, A., JANG, Y. J. & LESCHZINER, M. A. 2005 Comparative LES and unsteady RANS computations for a periodically-perturbed separated flow over a backward-facing step. *J. Fluids Eng.* **127** (5), 872–878.
- EVSTAFYEVA, O., MORGANS, A. S. & DALLA LONGA, L. 2017 Simulation and feedback control of the Ahmed body flow exhibiting symmetry breaking behaviour. *J. Fluid Mech.* **817**, R2.
- GEROPP, D. 1995 Process and device for reducing the drag in the rear region of a vehicle, for example, a road or rail vehicle or the like. United States Patent **US 5407245 A**.
- GEROPP, D. & ODENTHAL, H.-J. 2000 Drag reduction of motor vehicles by active flow control using the Coanda effect. *Exp. Fluids* **28** (1), 74–85.
- GILLIÉRON, P. & KOURTA, A. 2013 Aerodynamic drag control by pulsed jets on simplified car geometry. *Exp. Fluids* **54** (2), 1457.
- GRANDEMANGE, M., GROHLKE, M. & CADOT, O. 2013 Turbulent wake past a three-dimensional blunt body. Part 1. global modes and bi-stability. *J. Fluid Mech.* **722**, 51–84.
- GAD-EL HAK, M. 2006 *Flow Control: Passive, Active, and Reactive Flow Management*. Cambridge university press.
- HAN, X., KRAJNOVIĆ, S. & BASARA, B. 2013 Study of active flow control for a simplified vehicle model using the PANS method. *Int. J. Heat Fluid Flow* **42**, 139–150.
- HUCHO, W.-H. 2002 *Aerodynamik der stumpfen Körper. Physikalische Grundlagen und Anwendungen in der Praxis*, 2nd edn. Wiesbaden: Vieweg Verlag.
- KENNEDY, J. 2017 Particle swarm optimization. In *Encyclopedia of Machine Learning and Data Mining* (ed. C. Sammut & G. I. Webb), pp. 967–972. Boston, MA: Springer US.
- KIM, J. 2011 Physics and control of wall turbulence for drag reduction. *Phil. Trans. Roy. Soc. A* **369** (1940), 1396–1411.
- KOURTA, A. & LECLERC, C. 2013 Characterization of synthetic jet actuation with application to ahmed body wake. *Sensors and Actuators A: Physical* **192**, 13–26.
- KRAJNOVIĆ, S. 2009 Large eddy simulation of flows around ground vehicles and other bluff bodies. *Phil. Trans. R. Soc. A* **367** (1899), 2917–2930.
- KRENTEL, D., MUMINOVIC, R., NITSCHE, W. & KING, R. 2012 Influence of periodic-blowing actuators on the wake and the total drag of generic 3d car models. *Int. J. Flow Control* **4** (3), 97–108.
- LI, Y., CUI, W., JIA, Q. & YANG, Z. 2018 Wake control on a simplified vehicle using steady blowing. In *Proceedings of the 8th International Conference on Fluid Mechanics (ICFM8)*, pp. 1–6. Paper.
- MCKAY, M. D., BECKMAN, R. J. & CONOVER, W. J. 1979 Comparison of three methods for selecting values of input variables in the analysis of output from a computer code. *Technometrics* **21** (2), 239–245.
- MINELLI, G., KRAJNOVIĆ, S., NOACK, B. R. & BASARA, B. 2016 Active flow control of a frontstep with a rounded leading edge. *Flow, Turbul., Combust.* **97** (1), 1235–1254.
- MURALIDHARAN, K., MUDDADA, S. & PATNAIK, B. S. V. 2013 Numerical simulation of vortex induced vibrations and its control by suction and blowing. *Appl. Math. Model.* **37** (1-2), 284–307.
- NELDER, J. A. & MEAD, R. 1965 A simplex method for function minimization. *J. Comput.* **7**, 308–313.
- ÖSTH, J., KRAJNOVIĆ, S., NOACK, B. R., BARROS, D. & BORÉE, J. 2014 On the need for

- a nonlinear subscale turbulence term in POD models as exemplified for a high Reynolds number flow over an Ahmed body. *J. Fluid Mech.* **747**, 518–544.
- PARK, H., LEE, D., JEON, W.-P., HAHN, S., KIM, J., CHOI, J. & CHOI, H. 2006 Drag reduction in flow over a two-dimensional bluff body with a blunt trailing edge using a new passive device. *J. Fluid Mech.* **563**, 389–414.
- PASTOOR, M., HENNING, L., NOACK, B. R., KING, R. & TADMOR, G. 2008 Feedback shear layer control for bluff body drag reduction. *J. Fluid Mech.* **608**, 161–196.
- PFEIFFER, J. & KING, R. 2014 Linear parameter varying active flow control for a 3d bluff body exposed to cross-wind gusts. In *AIAA Paper, 2014-2406*.
- PRESS, W.H., FLAMERY, B.P., TEUKOLSKY, S.A. & VETTERLING, W.T. 2007 *Numerical Recipes, The Art of Scientific Computing*, 3rd edn. Cambridge, UK, etc.: Cambridge University Press.
- RECHENBERG, I. 1973 *Evolutionsstrategie: Optimierung technischer Systeme nach Prinzipien der biologischen Evolution*. Stuttgart: Frommann-Holzboog.
- RUSSELL, S. J. & NORVIG, P. 2016 *Artificial Intelligence: A Modern Approach*. Malaysia; Pearson Education Limited.
- SCHMIDT, H.-J., WOSZIDLO, R., NAYERI, C. N. & PASCHEREIT, C. O. 2015 The effect of flow control on the wake dynamics of a rectangular bluff body in ground proximity. *Exp. Fluids* **56**, article 151.
- VIKEN, S., VATSA, V., RUMSEY, C. & CARPENTER, M. 2003 Flow control analysis on the hump model with RANS tools. In *41st Aerospace Sciences Meeting and Exhibit*, p. 218.
- WAHDE, M. 2008 *Biologically Inspired Optimization Methods: An Introduction*. WIT Press.
- ZHANG, B. F., LIU, K., ZHOU, Y., TO, S. & TU, J. Y. 2018 Active drag reduction of a high-drag ahmed body based on steady blowing. *J. Fluid Mech.* **856**, 351–396.